










Polar phonons and magnetic excitations in the antiferromagnet CoF_2

R. M. Dubrovin ^{1,*} A. Tellez-Mora ² A. C. Garcia-Castro ³ N. V. Siverin ^{1,†}
N. N. Novikova ⁴ K. N. Boldyrev ⁴ E. A. Mashkovich ⁵ Aldo H. Romero ² and R. V. Pisarev ¹

¹*Ioffe Institute, Russian Academy of Sciences, 194021 St. Petersburg, Russia*

²*Department of Physics and Astronomy, West Virginia University,
WV-26506-6315 Morgantown, West Virginia, USA*

³*School of Physics, Universidad Industrial de Santander, 680002 Bucaramanga, Colombia*

⁴*Institute of Spectroscopy, Russian Academy of Sciences, 108840 Moscow, Troitsk, Russia*

⁵*Institute of Physics II, University of Cologne, 50937 Cologne, Germany*

(Dated: June 25, 2024)

The coupling between antiferromagnetic spins and infrared-active phonons in solids is responsible for many intriguing phenomena and is a field of intense research with extensive potential applications in the modern devices based on antiferromagnetic spintronics and phononics. Insulating rutile antiferromagnetic crystal CoF_2 is one of the model materials for studying nonlinear magneto-phononics due to the strong spin-lattice coupling as a result of the orbitally degenerate ground state of Co^{2+} ions manifested in the plethora of static and induced piezomagnetic effects. Here, we report results on the complete infrared spectroscopy study of lattice and magnetic dynamics in CoF_2 in a wide temperature range and their careful analysis. We observed that infrared-active phonons demonstrate frequency shifts at the antiferromagnetic ordering. Furthermore, using first-principles calculations, we examined the lattice dynamics and disclosed that these frequency shifts are rather due to the spin-phonon coupling than geometrical lattice effects. Next we found that the low-frequency dielectric permittivity demonstrates distinct changes at the antiferromagnetic ordering due to the spontaneous magnetodielectric effect caused by the behavior of infrared-active phonons. In addition, we have observed magnetic excitations in the infrared spectra and identified their magnetodipole origin. To strengthen our conclusions, we analyze the theoretical phonon-magnon coupling overall phonons at the Γ point. We conclude that the largest effect comes from the A_{1g} and B_{2g} Raman-active modes. As such, our results establish a solid basis for further investigations and more deeper understanding of the coupling of phonons with spins and magnetic excitations in antiferromagnets.

I. INTRODUCTION

Antiferromagnets are promising materials for next-generation spintronic devices because of their several considerable advantages over ferromagnets. These advantages cover, for example, orders of magnitude higher frequencies of spin dynamics (typically in the terahertz range), insensitivity to external magnetic perturbations, and the absence of stray field [1–11]. In turn, the coupling between the optical phonons with spins in antiferromagnets has tremendous interest and it is, nowadays, a hot topic area of modern condensed matter physics. The latter interest lies at the intersection of spintronics and phononics because it provides the attractive route to control of the magnetic and structural properties of materials [12–21]. Nevertheless, despite the intensive research in this area in recent years, the microscopic mechanisms for the spin-phonon coupling in insulator crystals remain poorly understood [22; 23].

Among magnetic crystals, $3d$ transition metal fluorides TF_2 , with a rutile structure, are attractive materials for antiferromagnetic spintronic applications. Thus, the spin

Seebeck effect was experimentally observed in thin films of MnF_2 [24] and FeF_2 [25] that can be used for generation of nonequilibrium magnons for spin caloritronic devices. The controllable generation of coherent spin currents at terahertz frequencies, due to the spin-pumping effect, has been demonstrated in thin film of MnF_2 [26]. It has been shown that phonon frequencies [27; 28] and dielectric permittivity in the MnF_2 [29; 30] are changed at the antiferromagnetic ordering that indicates a coupling of phonons with spins in the TF_2 materials.

The cobalt fluoride CoF_2 is one of the most fascinating TF_2 compounds because the Co^{2+} cation exhibits a not fully frozen orbital momentum with a strong spin-orbit interaction leading to an exceptionally high-magnetic anisotropy [31; 32] and large magnetostriction [33; 34]. Thus, the strong static [35–37], phonon-driven [38] and laser-induced THz [39; 40] piezomagnetic effects have been observed. Furthermore, CoF_2 has been a model material for nonlinear phononics and magneto-phononics in which it was discovered that infrared-active phonons and magnons pumped by terahertz pulses efficiently excite coherent Raman-active phonons [38; 41; 42]. It is worth mentioning that most of basic physical properties of this, as well as of some other TF_2 crystals, are fairly known. These studies include the experimental exploration of the magnetic and optical properties even considering experiments in the high magnetic field [43–47]. The latter studies partially cover the spin excitations and Raman-active phonons at the center of the Brillouin zone have

* dubrovin@mail.ioffe.ru; Also at University of Nizhny Novgorod, 603022 Nizhny Novgorod, Russia

† Now at Experimental Physics 2, Department of Physics, TU Dortmund, 44227, Dortmund, Germany

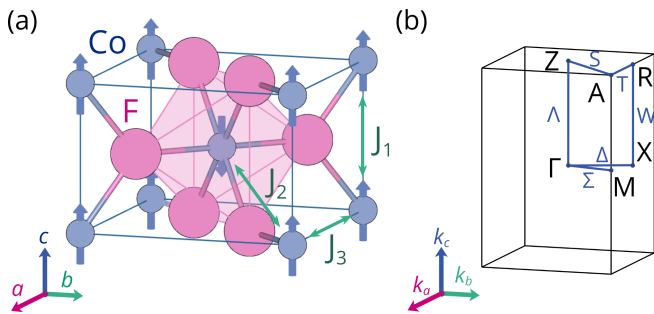


FIG. 1. (a) Crystal and magnetic structures of CoF_2 with tetragonal space group $P4_2/mnm$. The spins of Co^{2+} ions are antiferromagnetically ordered along the c axis as marked by arrows. The Co^{2+} ions in the unit cell are numbered. The dominant exchange interactions J_1 , J_2 , and J_3 are also marked. (b) The Brillouin zone of rutile indicating the high-symmetry $M-\Gamma-X-R-A-Z-\Gamma$ path used in the lattice dynamic and magnon calculations.

been investigated experimentally in a wide temperature range [48–55]. Nevertheless, there is a lack of understanding of the infrared-active phonons and magnetic-dipole active excitations in a wide range of temperatures and some studies only cover a few temperature points [56–58]. Moreover, the temperature behavior of dielectric properties of CoF_2 remains generally unexplored.

In this paper, we report the results of a detailed experimental study of the lattice and spin dynamics of CoF_2 in a wide temperature range by using far-infrared and dielectric spectroscopy techniques. The latter findings are supported by appropriate first-principles calculations and their careful analysis. We show that frequencies of the polar phonons present a clear shift at the antiferromagnetic ordering. Lattice dynamics calculations have shown that these frequency shifts are due to the spin-phonon coupling. Moreover, we have revealed that observed changes in the low-frequency dielectric permittivity at the antiferromagnetic ordering, due to the spontaneous magnetodielectric effect, are caused by the coupling of spins with polar phonons.

II. METHODS

A. Crystal and magnetic structures:

Cobalt fluoride CoF_2 crystallizes in a centrosymmetric tetragonal rutile crystal structure with the space group $P4_2/mnm$ (D_{4h}^{14} , #136, $Z = 2$) [59] as shown in Fig. 1(a). The lattice parameters measured at room temperature are $a = b = 4.695 \text{ \AA}$ and $c = 3.1817 \text{ \AA}$ [60]. The rutile structure consists of alternating neighboring CoF_6 octahedra which share edges and corners. The Co^{2+} and F^{1-} ions are located at the Wyckoff positions 2a (0, 0, 0) and 4f (0.30346, 0.30346, 0.0000) with site symmetries D_{2h} and C_{2v} , respectively [60]. The antiferromagnetic phase transition in CoF_2 takes place at

$T_N = 39 \text{ K}$ and the magnetic space group $P4_2'/mnm'$ is realized [61]. At low temperatures in the antiferromagnetic phase the spins $S = 3/2$ of Co^{2+} ($3d^7$) ions are aligned along the c axis with opposite directions at the center and corners [62–64] as shown by purple arrows in Fig. 1(a). The experimental magnetic structure of CoF_2 can be adequately described by the three exchange integrals between the nearest-neighboring Co^{2+} ions with values $J_1 = -0.15 \text{ meV}$, $J_2 = 1.6 \text{ meV}$, and $J_3 \sim 0 \text{ meV}$ [53] which are indicated in Fig. 1(a).

B. Experimental Details:

The single crystal of CoF_2 was grown by the Bridgman method in platinum crucibles in a helium atmosphere as described in Ref. [65]. Samples with the ab and ac planes were cut from the x-ray oriented single crystal and polished to optical quality. The surface size of the samples for far-infrared experiments were about $8 \times 8 \text{ mm}^2$ whereas the thicknesses were about 5 mm. Samples for dielectric experiments were prepared in a form of plane-parallel plates with a thickness of about 1.5 mm and an area of about 50 mm^2 .

The far-infrared (IR) reflectivity and transmission measurements were carried out in the spectral range $50\text{--}650 \text{ cm}^{-1}$ and $30\text{--}300 \text{ cm}^{-1}$, respectively, using Bruker IFS 125HR spectrometer with a liquid helium-cooled bolometer. The ac plane sample was mounted on a cold finger of a closed-cycle helium cryostat Cryomech ST403. The polarization of electric field \mathbf{E} was switched between two positions of the linear thin film polarizer along the a and c axes of the crystal. In reflectivity measurements, the incident light beam was at 10° from the normal to the sample plane. The relative reflectivity spectra from the sample with respect to a reference reflectivity of a gold mirror at room temperature were measured at slow continuous cooling from 300 to 5 K. No corrections on the surface quality and shape of the sample, as well as change of positions due to cold finger thermal contraction, were done. The absolute reflectivity spectra were obtained by means of the Bruker IFS 66v/S spectrometer in the range of $50\text{--}7500 \text{ cm}^{-1}$ in order to determine the values of high-frequency dielectric permittivity ϵ_∞ .

The dielectric permittivity ϵ^{lf} in the frequency range from 20 Hz to 1 MHz was measured using precision RLC meter AKTAKOM AM-3028. The ab and ac plane samples were used to measure the dielectric permittivity ϵ^{lf} along the a ($a = b$) and c axes, respectively. Electric contacts were deposited on the sample surfaces using silver paint to form a capacitor. Samples were placed in a helium flow cryostat Cryo CRC-102 and capacitance measurements were performed at continuous heating from 5 to 300 K. Experimental data are presented only for the frequency of 100 kHz because no noticeable dispersion was observed in the studied frequency range. The dielectric losses are very small, on the order of 10^{-5} , and

no noticeable temperature changes were detected.

C. Computational Details:

The obtained experimental results were supplemented by the lattice dynamic calculations within the density-functional theory (DFT) framework [66; 67] and the projector-augmented wave method [68] as implemented in the Vienna *ab initio* simulation package (VASP) [69; 70]. The configurations considered in the pseudopotentials for the valence electrons were Co ($3p^6 3d^7 4s^2$, version 23Apr2009) and F ($2s^2 2p^5$, version 08Apr2002). The Monkhorst-Pack scheme with a mesh $6 \times 6 \times 8$ has been employed for the Brillouin zone integration [71]. As such, an $E_{\text{cut}} = 600$ eV energy cutoff was used to give forces convergence of less than $0.001 \text{ eV} \cdot \text{\AA}^{-1}$. The exchange-correlation energy was represented within the generalized gradient approximation (GGA) in the Perdew-Burke-Ernzerhof revised for solids PBEsol form [72]. The GGA + U + J approximation within the Dudarev's formalism [73] with the on-site Coulomb interaction $U = 6.0$ eV and an exchange correction $J = 1.0$ eV were used to account for the strong correlation between electrons in the $3d^7$ shell of the Co^{2+} ions [74]. The dielectric constants, phonon dispersions, eigenvectors, and Born effective charges were calculated within the density-functional perturbation theory [75] and analyzed through the PHONOPY code [76]. The longitudinal-transverse optical (LO-TO) phonon splitting near the Γ -point was included using nonanalytical corrections to the dynamical matrix [77]. Finally, the correlation between eigendisplacements of the LO and TO modes was evaluated using LADYTOOLS [78]. Moreover, we use the LKAG Green's function method [79] as implemented in the TB2J code [80] to calculate the exchange interaction constants of CoF_2 following the process described in Ref. [81]. Particularly, we interface TB2J with the Siesta package [82], where we use a 400 Ry mesh-cutoff energy and a double-zeta polarized basis in addition to the previously mentioned DFT parameters. We compare the LKAG results with those obtained from VASP with an energy mapping procedure. Finally, we use linear spin-wave theory [83] to calculate the magnon frequencies.

III. RESULTS AND DISCUSSION

A. Far-infrared spectroscopy:

The group-theoretical analysis for the rutile CoF_2 predicts 13 phonon modes at the Γ point of the Brillouin

zone [84]:

$$\Gamma_{\text{total}} = \underbrace{A_{2u} \oplus E_u}_{\Gamma_{\text{acoustic}}} \oplus \underbrace{A_{1g} \oplus B_{1g} \oplus B_{2g} \oplus E_g}_{\Gamma_{\text{Raman}}} \oplus \underbrace{A_{2u} \oplus 3E_u}_{\Gamma_{\text{IR}}} \oplus \underbrace{A_{2g} \oplus 2B_{1u}}_{\Gamma_{\text{Silent}}}, \quad (1)$$

among which there are 2 acoustic $\Gamma_{\text{acoustic}} = A_{2u} \oplus E_u$, three ‘‘silent’’ $\Gamma_{\text{silent}} = A_{2g} \oplus 2B_{1u}$, four Raman-active $\Gamma_{\text{Raman}} = A_{1g} \oplus B_{1g} \oplus B_{2g} \oplus E_g$, and four infrared-active (polar) $\Gamma_{\text{IR}} = A_{2u} \oplus 3E_u$ phonons. The A and B modes are nondegenerated, whereas the E modes are doubly degenerated. The polar A_{2u} phonon is polarized along the c axis whereas $3E_u$ phonons are active in the ab plane.

The IR reflectivity spectra at room temperature with the polarization \mathbf{E} of light parallel to the a and c axis are shown in Figs. 2(a) and 2(b), respectively. Three and one reflection bands are observed in the spectra for nonequivalent polarizations, which correspond to the E_u ($\mathbf{E} \parallel a$) and A_{2u} ($\mathbf{E} \parallel c$) polar phonons in full agreement with group theory predictions. To obtain the phonon parameters the reflectivity spectra $R(\omega)$ were fitted using the Fresnel equation [85]

$$R(\omega) = \left| \frac{\sqrt{\varepsilon(\omega)} - \sqrt{\mu(\omega)}}{\sqrt{\varepsilon(\omega)} + \sqrt{\mu(\omega)}} \right|^2, \quad (2)$$

with the factorized form of the complex dielectric permittivity [86]

$$\varepsilon(\omega) = \varepsilon_1(\omega) - i\varepsilon_2(\omega) = \varepsilon_\infty \prod_j^N \frac{\omega_{j\text{LO}}^2 - \omega^2 + i\gamma_{j\text{LO}}\omega}{\omega_{j\text{TO}}^2 - \omega^2 + i\gamma_{j\text{TO}}\omega}, \quad (3)$$

where ε_∞ is the high-frequency dielectric permittivity, $\omega_{j\text{LO}}$, $\omega_{j\text{TO}}$, $\gamma_{j\text{LO}}$ and $\gamma_{j\text{TO}}$ correspond to LO and TO frequencies (ω_j) and dampings (γ_j) of the j th polar phonon, respectively. Multiplication occurs over all N polar phonons which are active for the relevant polarization of light. Far from the magnetic excitations, it is assumed that magnetic permeability $\mu \equiv 1$. There is, in general, a good agreement between experimental green and fit black lines, as shown in Figs. 2(a) and 2(b). Slight deviations appear at the highest-frequency phonons presumably due to multiphonon absorption [87]. The real ε_1 and imaginary ε_2 parts of the complex dielectric functions $\varepsilon = \varepsilon_1 - i\varepsilon_2$ which correspond to the fits are shown in Figs. 2(c) and 2(d). The obtained parameters of the polar phonons from fits using Eqs. (2) and (3) of the experimental data at room temperature are listed in Table I. These parameters are in fair agreement with the literature data for CoF_2 [56; 57]. Note that LO-TO splitting does not depend on the degeneracy of polar phonons [88].

To reveal the temperature evolution of the polar phonons in CoF_2 , we perform the measurements of the infrared reflectivity in the range from 5 to 300 K for both polarizations which are shown by the color maps

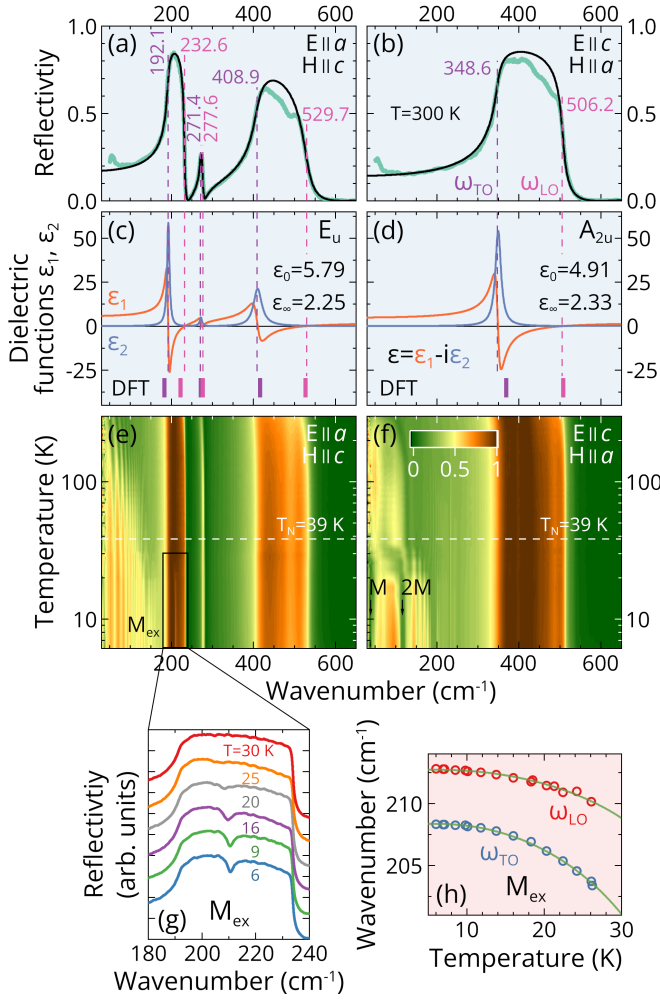


FIG. 2. IR reflectivity spectra with the electric field of light \mathbf{E} polarized along (a) a and (b) c axes in the ac plane for CoF₂ at room temperature. The black lines are fits based on a generalized oscillator model according to Eq. (3). Real ϵ_1 and imaginary ϵ_2 parts of the dielectric functions corresponding to the (c) E_u and (d) A_{2u} polar phonons. Colored dashed lines indicate the experimental ω_{TO} and ω_{LO} phonon frequencies which are indicated. Colored sticks on the (c) and (d) panels present the calculated frequencies of polar phonons. Temperature maps of IR reflectivity spectra for the light polarizations (e) $\mathbf{E} \parallel a$ and (f) $\mathbf{E} \parallel c$. Magnon (M), two-magnon (2M) and magnetic M_{ex} excitations are marked. (g) Effect of magnetic excitation M_{ex} on the reflectivity spectra at the indicated temperatures. (h) Temperature dependencies of frequencies of the magnetic excitation M_{ex} .

in Figs. 2(e) and 2(f). The bright vertical brown bands correspond to polar phonons and it can be seen that their evolution with temperature is not significant. It should be noted that we did not detect in CoF₂ any evidences of the exchange driven phonon splitting below T_N which was previously observed in the antiferromagnetic cubic transition-metal monoxides and oxide spinels [89–92]. We attribute the absence of clear signs of the exchange driven phonon splitting in the antiferromagnetic

rutiles CoF₂ and MnF₂ from Ref. [28] to the fact that they have tetragonal crystal structure and they have no magnetic frustration, which is apparently essential for this effect.

Further, the obtained reflectivity spectra were analyzed using Eqs. (2) and (3). The derived temperature dependences of the TO and LO frequencies of E_u and A_{2u} polar phonons are shown on a logarithmic scale in Figs. 3(a) and 3(b). In the paramagnetic state $T > T_N$, the TO and LO frequencies ω of all polar phonons increase (*i.e.* harden) at cooling. It should be noted that the hardening of phonon frequencies is typical for conventional insulator crystals due to anharmonic effects which manifest themselves in the compression of the crystal at cooling [93]. In turn, a decrease in the distance between ions in a crystal leads to an increase of the interaction forces k between them, which drives an increase of the phonon frequencies $\omega \sim \sqrt{k/\mu}$, where μ is a reduced mass [94]. According to the Ref. [34] the lattice parameters of CoF₂ decrease at cooling in the paramagnetic phase. The observation in the isostructural antiferromagnet MnF₂ presents a fascinating phenomenon where, contrary to typical behavior, the frequency $\omega_{1\text{TO}}$ of the polar phonon exhibiting E_u symmetry decreases on cooling. This anomaly underscores a unique aspect of phonon behavior in antiferromagnetic materials, challenging conventional understandings and inviting a deeper investigation into the underlying mechanisms [28].

It is clearly seen in Fig. 3 that the temperature dependencies of all polar phonons abruptly change the smooth behavior at the Néel temperature $T_N = 39$ K evidencing the influence of the spin-phonon coupling. For a deeper understanding of this effect, we fitted the temperature dependencies of phonon frequencies in the paramagnetic state using expression describing the three- and four-phonon anharmonic processes [95; 96]

$$\omega^{\text{NM}}(T) = \omega_0 + A \left(1 + \frac{2}{e^{\hbar\omega_0/2k_B T} - 1} \right) + B \left(1 + \frac{3}{e^{\hbar\omega_0/3k_B T} - 1} + \frac{3}{(e^{\hbar\omega_0/3k_B T} - 1)^2} \right), \quad (4)$$

TABLE I. Experimental TO and LO frequencies ω_j (cm⁻¹), dampings γ_j (cm⁻¹) and dielectric strengths $\Delta\epsilon_j$ of the polar phonons, static ϵ_0 and high-frequency ϵ_∞ dielectric permittivities in CoF₂ at room temperature. For comparison, the calculated frequencies for the nonmagnetic state are also given in parentheses.

Sym.	j	$\omega_{j\text{TO}}$	$\gamma_{j\text{TO}}$	$\omega_{j\text{LO}}$	$\gamma_{j\text{LO}}$	$\Delta\epsilon_j$
E_u	1	192.1 (182.7)	7.0	232.6 (222.3)	4.2	2.14 (2.26)
	2	271.4 (271.8)	6.7	277.6 (276.2)	5.3	0.12 (0.103)
	3	408.9 (415.7)	24.5	529.7 (526.9)	28.1	1.28 (1.33)
		$\epsilon_\infty = 2.25$ (2.54)		$\epsilon_0 = 5.79$ (6.24)		
A_{2u}	1	348.6 (369.8)	16.6	506.2 (507.1)	13.0	2.58 (2.32)
			$\epsilon_\infty = 2.33$ (2.63)		$\epsilon_0 = 4.91$ (4.95)	

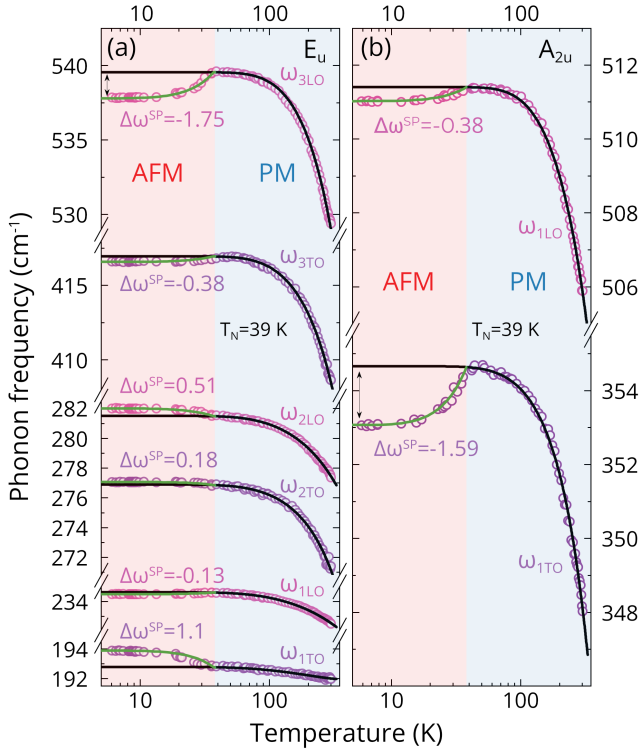


FIG. 3. Temperature dependences of frequencies ω of the (a) E_u and (b) A_{2u} polar phonons in CoF_2 on a logarithmic scale. The color circles are experimental data. The black lines corresponds to the fit under the assumption of the anharmonic temperature behavior only according to Eq (4). The green lines are fits of the frequency shift due to the spin-phonon coupling according to Eqs. (5), (6). The antiferromagnetic and paramagnetic phases are shown in the red- and blue-filled backgrounds, respectively.

where ω_0 is harmonic phonon frequency, A and B are parameters. It is worth noting that the phonon anharmonicity in the real crystals is very complicated, but Eq. (4) gives reasonable fits above T_N as shown by the black lines in the Fig. 3. The frequency shifts of the phonon frequencies from extrapolated anharmonic behavior in the antiferromagnetic phase were fitted by the function [97]:

$$\omega^{\text{AFM}}(T) = \omega^{\text{NM}}(T) + \Delta\omega^{\text{SP}}M^2(T), \quad (5)$$

where $\Delta\omega^{\text{SP}}$ is the spin-phonon coupling constant which is equal to the phonon frequency at the low temperature and M is the magnetic order parameter. Neglecting the short-range magnetic ordering above T_N , the temperature dependence of M can be estimated by using the Brillouin function [98] such as:

$$M(x) = M_0 \left[\frac{2S+1}{2S} \coth\left(\frac{2S+1}{S}x\right) - \frac{1}{2S} \coth\left(\frac{x}{2S}\right) \right], \quad (6)$$

where $x = \frac{3S}{S+1} \frac{M T_N}{T}$, S is spin value of the magnetic

ion, and M_0 is the full magnetic order parameter. There is a fair agreement between fits using Eqs. (5), (6) and experimental data below T_N as shown in Fig. 3. The obtained values of the spin-phonon coupling constants $\Delta\omega^{\text{SP}}$ given in Fig. 3 are close to the published data for Raman-active phonons [97]. It is worth nothing that spin-phonon coupling for IR-active TO phonons has been reported for the isostructural antiferromagnet MnF_2 [28].

Here, it can be observed that the temperature maps of the IR reflectivity spectra reveal features at about 37, 115, and 209 cm^{-1} appearing at antiferromagnetic ordering, as it can be seen in Figs. 2(e) and 2(h). According to the numerous published data, the feature at 37 cm^{-1} corresponds to the magnon excitation with symmetry $\Gamma_3^+ + \Gamma_4^+$, 115 cm^{-1} ($\Gamma_4^+ + \Gamma_5^+$) is two-magnon mode, and 209 cm^{-1} (Γ_2^+) is magnetic exciton [49–53; 55; 99–102]. Magnetic excitons in CoF_2 are usually considered as a transition between the split by crystal and exchange fields, and the spin-orbit coupling of Co^{2+} ions levels [49; 100; 103; 104]. At that the magnetic exciton with the lowest frequency is a magnon. It is interesting that the magnetic excitation M_{ex} with frequency 209 cm^{-1} is located in the Reststrahlen band between 2TO and 2LO frequencies of the polar E_u phonon and appears by a dip in the reflection spectra, as shown in Figs. 2(e) and 2(g), and it was previously discovered in Ref. [58]. Note that, this magnetic excitation M_{ex} appears in the polarized IR reflectivity spectra on the polar E_u phonon only at $\mathbf{E} \parallel a$, $\mathbf{H} \parallel c$ in the ac plane and does not appear at $\mathbf{E} \parallel a$, $\mathbf{H} \parallel b$ in the ab plane [58; 105] which confirms its magnetodipole character.

To reveal the temperature dependence of the frequency of this magnetic excitation M_{ex} , the feature on the IR reflection spectra was fitted using Eqs. (2), (3) and magnetic permeability in the form which is close to the Eq. (3) [105]

$$\mu(\omega) = \mu_1(\omega) - i\mu_2(\omega) = \frac{\omega_{\text{LO}}^2 - \omega^2 + i\gamma_{\text{LOW}}}{\omega_{\text{TO}}^2 - \omega^2 + i\gamma_{\text{TO}\omega}}, \quad (7)$$

where ω_{LO} and ω_{TO} correspond to LO and TO frequencies of the magnetic excitation. The recieved temperature dependences of ω_{LO} and ω_{TO} frequencies of the M_{ex} and fit lines obtained using Eq. (6) are shown in Fig. 2(h) according to Ref. [106].

At low temperatures, the CoF_2 crystal becomes more transparent in the low-frequency region below 200 cm^{-1} (see Fig. 4). The reflection from the back side of the sample with double absorption at its thickness and interference are added to the reflection from the front side as shown in Figs. 2(e) and 2(f). Thus, the absorption related to magnon M at 37 cm^{-1} and two-magnon 2M excitation at 115 cm^{-1} are observed in the spectra with $\mathbf{E} \parallel c$, $\mathbf{H} \parallel a$ as can be seen in Figs. 2(f) and Figs. 4(b). In addition to the magnon M , and the two-magnon 2M already described, four narrow absorption lines at temperatures both above and below T_N were also observed in the transmission spectrum with $\mathbf{E} \parallel c$, $\mathbf{H} \parallel a$, as shown in Fig. 4(b).

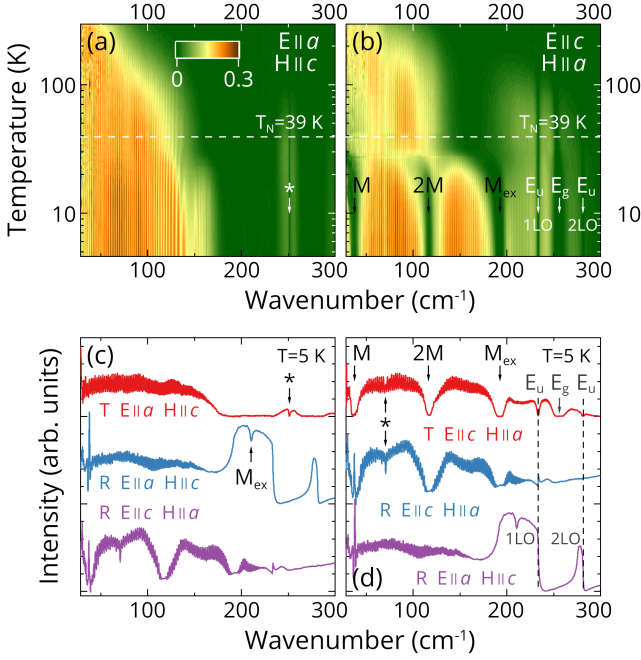


FIG. 4. Temperature maps of the IR transmission spectra for CoF₂ for the light polarization (a) $\mathbf{E} \parallel a$ and (b) $\mathbf{E} \parallel c$ in the ac plane. Additionally, the transmission (T) and reflection (R) spectra at $T = 5$ K for the light polarization are presented for (c) $\mathbf{E} \parallel a$ and (d) $\mathbf{E} \parallel c$ along with the reflection spectra for another polarization in the ac plane. The detected excitations are described in the text.

Absorption at 193 cm^{-1} corresponds to another magnetic excitation M_{ex} with symmetry $\Gamma_3^+ + \Gamma_4^+$ [49; 50; 100–102]. Lines at 234 and 282 cm^{-1} are 1LO and 2LO frequencies of polar phonons with E_u symmetry. Note that the absorption bands corresponding to LO polar phonons begin to be observed in the spectra at temperatures significantly higher than T_N [see Fig. 4(b)]. According to the crystal symmetry, the E_u phonons are active at $\mathbf{E} \parallel a$. In the reflection spectrum, these off-symmetry LO modes also appear in forbidden polarizations as shown in Fig. 4(d). This effect occurs in uniaxial crystals in the infrared reflectivity spectra at the off-normal incidence of radiation with the p -polarization [107]. We observe the appearance of this effect in the transmission spectra.

It is interesting to note that the absorption band at 256 cm^{-1} corresponds to the Raman-active E_g phonon which is infrared inactive. Magnetodipole absorption of this Raman-active phonon was previously experimentally observed in CoF₂ and it is due to the coupling of magnetic excitations with the E_g mode [101; 102; 108–111]. Moreover, the magnetodipole phonon absorption begins at temperatures well above T_N , as in the previously reported papers [see Fig. 4(b)]. Also, a slight absorption is observed at low temperatures at 71 cm^{-1} as shown by an asterisk in Fig. 4(d). The frequency of these features is close to the Raman-active B_{1g} phonon at 65 cm^{-1} , but it is most likely an artifact and is unlikely to be related.

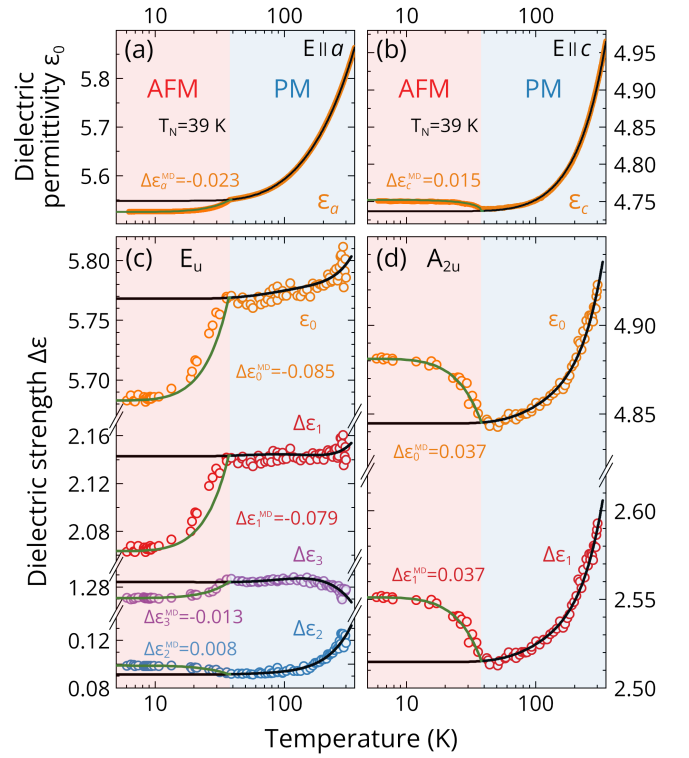


FIG. 5. Temperature dependences of the low-frequency dielectric permittivity ε^{lf} along the (a) a and (b) c axes, the dielectric strengths $\Delta\varepsilon_j$ and static dielectric permittivity ε_0 of the (c) E_u and (d) A_{2u} polar phonons. The open color circles correspond to the experimental data. The black and green lines are fitted, assuming the anharmonic and spontaneous magnetodielectric effects. Values of the spontaneous magnetodielectric coupling parameter $\Delta\varepsilon^{\text{MD}}$ are given. The antiferromagnetic and paramagnetic phases are shown in the red- and blue-filled backgrounds, respectively.

Weak but distinct absorption line at 251 cm^{-1} was detected on the transmission spectra with $\mathbf{E} \parallel a$, $\mathbf{H} \parallel c$ below $T = 90$ K [see Fig. 4(a)]. This line is close to the Raman-active E_g phonon at 256 cm^{-1} . Still, any absence of temperature dependence indicates that it is related to the small amount of water in the cryostat, and not with the sample under study. Thus, the CoF₂ possesses several electro-dipole and magnetodipole excitations with rich physics manifested in the infrared spectra.

B. Dielectric properties:

It is well known that the static dielectric permittivity $\varepsilon_0 = \varepsilon_\infty + \sum_j \Delta\varepsilon_j$ of crystals is related to the j th polar phonon through its dielectric strength $\Delta\varepsilon_j$ according to the expression [112]:

$$\Delta\varepsilon_j = \frac{\varepsilon_\infty}{\omega_{j\text{TO}}^2} \frac{\prod_k \omega_{k\text{LO}}^2 - \omega_{j\text{TO}}^2}{\prod_{k \neq j} \omega_{k\text{TO}}^2 - \omega_{j\text{TO}}^2}. \quad (8)$$

The static ε_0 , high frequency ε_∞ dielectric permittivities, and dielectric strengths $\Delta\varepsilon$ evaluated from reflectivity spectra at room temperature using Eq. (8) are listed in Table I and in Figs. 2(c) and 2(d). We observed that our obtained values of the dielectric parameters are in fair agreement with previously published data [56; 57].

The temperature behavior of the dielectric permittivity ε^{lf} at frequencies (about 1 MHz) much lower than lattice excitations represents the general temperature trend of the dielectric strengths of polar phonons. Figures 5(a) and 5(b) show experimental temperature dependencies of the low-frequency dielectric permittivities $\varepsilon^{\text{lf}}(T)$ measured in CoF₂ along the *a* and *c* axes, respectively. At all temperatures the relation $\varepsilon_a^{\text{lf}}(T) > \varepsilon_c^{\text{lf}}(T)$ holds. The values $\varepsilon_a^{\text{lf}}$ and $\varepsilon_c^{\text{lf}}$ at room temperature are close to those obtained from reflectivity spectra (see Table I). The low-frequency dielectric permittivities $\varepsilon_a^{\text{lf}}$ and $\varepsilon_c^{\text{lf}}$ decrease at cooling in the paramagnetic phase along both axes and the relative magnitude of these changes is comparatively tiny and amounts about 3%. Note that the similar temperature behavior of the low-frequency dielectric permittivity ε^{lf} was previously observed in the isostructural diamagnetic crystal ZnF₂ [113]. Moreover, this temperature behavior of the dielectric permittivity $\varepsilon^{\text{lf}}(T)$ is typical for conventional dielectric crystals [113–116].

At the Néel temperature $T_N = 39$ K both temperature dependencies of the dielectric permittivity $\varepsilon^{\text{lf}}(T)$ exhibit kinks due to the spontaneous magnetodielectric effect, as shown in Figs. 5(a) and 5(b). Below T_N the value of $\varepsilon_a^{\text{lf}}$ decreases, while $\varepsilon_c^{\text{lf}}$, on the contrary, increases at cooling [see Figs. 5(a) and 5(b)]. It is worth mentioning that similar temperature behavior of the $\varepsilon_a^{\text{lf}}$ and $\varepsilon_c^{\text{lf}}$ below T_N was previously observed in the isostructural antiferromagnet MnF₂ [29; 30]. To extract the spontaneous magnetodielectric effect, the temperature behavior above T_N was fitted by an Einstein-type function [29; 30; 117; 118]:

$$\varepsilon_{\text{NM}}^{\text{lf}}(T) = \varepsilon_0^{\text{lf}} + \frac{A}{e^{\hbar\omega^*/k_B T} - 1}, \quad (9)$$

where $\varepsilon_0^{\text{lf}}$ is the temperature independent low-frequency dielectric permittivity, A is constant, ω^* is the frequency of the “effective” polar phonon. The fit results using Eq. (9) which are shown by black lines in Figs. 5(a) and 5(b) allow us to extrapolate the “pure” low-frequency dielectric permittivity to the antiferromagnetic phase. The differences between experimental and fit lines give the magnetic contribution caused by the spontaneous magnetodielectric effect according to expression that is close to the Eq. (5):

$$\varepsilon^{\text{lf}}(T) = \varepsilon_{\text{NM}}^{\text{lf}}(T) + \Delta\varepsilon^{\text{MD}} M^2(T), \quad (10)$$

where $\Delta\varepsilon^{\text{MD}}$ is a coefficient defining the spontaneous magnetodielectric effect, and M is described by Eq. (6). There is a good agreement between experimental results and fits using Eq. (10) below T_N as shown by green lines in Figs. 5(a) and 5(b). The obtained values of the $\Delta\varepsilon_a^{\text{MD}}$ and $\Delta\varepsilon_c^{\text{MD}}$ listed in Figs. 5(a) and 5(b), respectively, are

somewhat less than those for MnF₂ from literature [29] which we can attribute to the difference in the values of the ion spins $S = 3/2$ for Co²⁺ and $5/2$ for Mn²⁺.

To reveal the contribution of each polar phonon to the $\Delta\varepsilon^{\text{MD}}$ we calculate the dielectric strengths $\Delta\varepsilon$ using experimental and fit TO and LO phonon frequencies at different temperatures by employing Eq. (8). The obtained temperature dependencies of the dielectric strengths $\Delta\varepsilon(T)$ of the E_u and A_{2u} polar phonons and the static dielectric permittivities ε_0 along the *a* and *c* axes are shown in Figs. 5(a) and 5(b), respectively. We assumed that the high-frequency dielectric permittivity temperature changes ε_∞ are insignificant and can be neglected [119; 120]. It is seen that at the antiferromagnetic ordering the clear shifts of the dielectric strengths $\Delta\varepsilon$ for all polar phonons are observed. These shifts $\Delta\varepsilon^{\text{MD}}$ are a manifestation of the spontaneous magnetodielectric effect caused by frequency changes of the polar phonons $\Delta\omega^{\text{SP}}$ due to the spin-phonon coupling. Note that the $\Delta\varepsilon_2^{\text{MD}}$ for the medium frequency E_u and lowest frequency A_{2u} polar phonons have a positive sign, while the $\Delta\varepsilon_1^{\text{MD}}$ and $\Delta\varepsilon_3^{\text{MD}}$, on the contrary, are positive as shown in Figs. 5(a) and 5(b). A fair qualitative agreement is observed between the temperature behavior of the low-frequency $\varepsilon^{\text{lf}}(T)$ and the static $\varepsilon_0(T)$ dielectric permittivities and their shifts below T_N due to the spontaneous magnetodielectric effect $\Delta\varepsilon^{\text{MD}}$ as can be seen in Fig. 5. Thus, we have shown that the shifts of the macroscopic dielectric permittivity $\Delta\varepsilon^{\text{MD}}$ at antiferromagnetic ordering are caused by changes of the frequencies $\Delta\omega^{\text{SP}}$ of microscopic polar phonons.

C. Lattice dynamics:

Aiming to explore the origin of the observed spin-phonon coupling, we performed several first-principles calculations of the lattice dynamics landscape in the

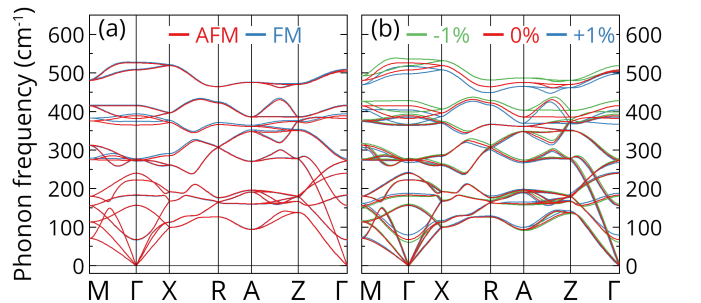


FIG. 6. Computed phonon dispersion curves along the M– Γ –X–R–A–Z– Γ high-symmetry path of the Brillouin zone of the CoF₂ for (a) antiferromagnetic (AFM) and ferromagnetic (FM) ordering, and (b) *ab* plane biaxial epitaxial strain -1%, 0%, +1%. Negative and positive signs of epitaxial strain correspond to the compression and expansion of the crystal, respectively.

CoF₂ in the antiferromagnetic (AFM) and ferromagnetic (FM) spin configurations considering the same lattice parameters as $a = b = 4.678 \text{ \AA}$ and $c = 3.154 \text{ \AA}$. Because the nonmagnetic (NM) phase is not accessible for DFT calculations of magnetic crystals, we assumed as a reference that $\omega^{\text{NM}} = (\omega^{\text{AFM}} + \omega^{\text{FM}})/2$ [28; 121]. The calculated phonon dispersion curves in the whole Brillouin zone for AFM (in red curves) and FM (in blue curves) spin configurations are shown in Fig. 6(a). The M- Γ -X-R-A-Z- Γ high-symmetry path shown in Fig. 1(b) was used in the lattice dynamics calculations. It is clearly seen that there are no significant differences between AFM and FM phonon dispersion curves which are consistent with the obtained values of the frequency shifts $\Delta\omega^{\text{SP}}$ of about 1 cm^{-1} in the experiment. According to the Ref. [122], the difference between FM and AFM phonon dispersion curves is related to the second derivative from exchange interactions with respect to the ionic displacements, which is presumably small in rutiles with respect to other magnetic materials. Note that the calculated phonon frequencies are real (positive) in the whole Brillouin zone and therefore CoF₂ in $P4_2/mnm$ space group is stable for both specified magnetic states.

The calculated frequencies ω of the optical phonons in AFM, FM, and NM states at the center of the Brillouin zone and estimated values of frequency shifts below T_N ($\Delta\omega^{\text{SP}} = \omega^{\text{AFM}} - \omega^{\text{NM}}$) are listed in Table II. The phonon frequencies are in fair agreement with previously reported calculations [124], experiments [55–58; 97], and our data from Table I. Signs and magnitudes of $\Delta\omega^{\text{SP}}$ for polar phonons obtained in our calculation agree with our experimental findings shown in Fig. 3. Thus, in these both cases $\Delta\omega^{\text{SP}}$ have positive sign for $\omega_{1\text{TO}}$, $\omega_{1\text{LO}}$, $\omega_{2\text{TO}}$, and $\omega_{2\text{LO}}$ frequencies of the E_u phonon and negative sign for

TABLE II. Calculated frequencies (cm^{-1}) of the infrared (IR), Raman-active (R), and silent (S) optical phonons for antiferromagnetic (AFM), ferromagnetic (FM), and nonmagnetic (NM) states together with spin-phonon coupling parameter (SP = AFM - NM) in CoF₂.

Act.	Sym.	Phonon	AFM	FM	NM	SP
IR	E_u	$\omega_{1\text{TO}}$	183.26	182.08	182.67	0.59
		$\omega_{1\text{LO}}$	222.29	222.22	222.25	0.04
		$\omega_{2\text{TO}}$	272.32	271.32	271.82	0.5
		$\omega_{2\text{LO}}$	276.65	275.72	276.19	0.47
		$\omega_{3\text{TO}}$	414.95	416.52	415.74	-0.78
		$\omega_{3\text{LO}}$	525.81	527.93	526.87	-1.06
	A_{2u}	$\omega_{1\text{TO}}$	364.82	374.72	369.77	-4.95
	$\omega_{1\text{LO}}$	504.47	509.74	507.11	-2.63	
R	B_{1g}		67.78	66.63	67.2	0.58
	E_g		273.16	277.35	275.25	-2.1
	A_{1g}		381.8	381.88	381.84	-0.04
	B_{2g}		507.65	509.51	508.58	-0.93
S	B_{1u}		156.74	156.34	156.54	0.2
	A_{2g}		239.8	240.13	239.96	-0.17
	B_{1u}		389	393.78	391.4	-2.39

other E_u and A_{2u} phonons. For Raman-active phonons in CoF₂ there is fair agreement between the experiment from Ref. [97] and our simulation for B_{1g} , A_{1g} , and B_{2g} phonons, whereas $\Delta\omega^{\text{SP}}$ for E_g phonon has different sign. However, it is worth noting that the spin-phonon frequency shift $\Delta\omega^{\text{SP}}$ for the E_g phonon in CoF₂ is different from those in MnF₂, FeF₂, and NiF₂ [97]. Besides, the $\Delta\omega^{\text{SP}}$ for the polar 3TO phonon of E_u symmetry has an opposite sign in CoF₂ and MnF₂ [28], which also indicates a difference in the spin-phonon coupling mechanism in these antiferromagnets. Therefore, the lattice dynamic simulation shows that the magnetic ordering shifts the phonon frequencies without changing unit cell volume of CoF₂.

Next, we calculate eigenvectors for all-optical phonons in the Brillouin zone’s center, shown in Fig. 7. The obtained ion displacements for phonons in CoF₂ are close to the same ones in isostructural rutile TiO₂ [125]. As can be seen in Fig. 7(b), the Co ions remain unmoved for all Raman-active and A_{2g} silent phonons. This is due to the fact that from symmetry the Co (2a) ions are active only for *ungerade* $A_{2u} \oplus E_u \oplus B_{1u}$ modes, while the F (4f) ions are involved for both *gerade* and *ungerade* phonons [84]. The ion displacement for most phonons are in the ab plane and only for the A_{2u} and B_{1u} vibrations are they along the c axis, as shown in Fig. 7. Besides, we see that the phonon displacements do not change the distances between the nearest-neighborhood Co ions and thus does not significantly modulate the exchange interaction. This in turn manifests itself in a small frequency shift due to the spin-phonon coupling and an insignificant difference between FM and AFM phonon dispersion curves in Fig. 6. Thus, we can conclude that the rutile structure does not favor significant spin-phonon interaction, which is confirmed experimentally by us on CoF₂ and on MnF₂ from Ref. [28].

To assign LO to TO polar phonons we expand the eigenvector of the m th LO mode to a linear combination of the TO normal modes $|\xi_m^{\text{LO}}\rangle = \sum_n C_{mn} |\xi_n^{\text{TO}}\rangle$ [126; 127]. Figure 8 shows the overlap matrix $C_{mn} = \langle \xi_m^{\text{LO}} | \xi_n^{\text{TO}} \rangle$, which represents the degree of correlation between eigenvectors of the m th LO and n th TO polar phonons. There is the “LO-TO rule” according to which in most crystals the sequence of polar phonons is such that the TO frequency is followed by LO frequency, with $\omega_{\text{LO}} > \omega_{\text{TO}}$ for each main crystallographic axis [128]. In the isostructural rutile TiO₂, which is an incipient ferroelectric, a more complex pattern of the correlation matrix C_{mn} is observed, polar phonons are significantly mixed by the strong Coulomb interaction, and the “LO-TO rule” was not fully obeyed [125]. Conversely, the “LO-TO rule” is satisfied for all polar phonons in CoF₂ and LO is more correlated with the nearest TO mode of the same symmetry with $\omega_{\text{TO}} < \omega_{\text{LO}}$. Moreover, since the A_{2u} polar phonon is the single one, the eigenvectors $|\xi^{\text{TO}}\rangle = |\xi^{\text{LO}}\rangle$ ($C = 1$) are equal and ion displacements for this TO and LO modes are the same as can be seen in Fig. 7(a). Nonetheless, despite this fact, the frequency

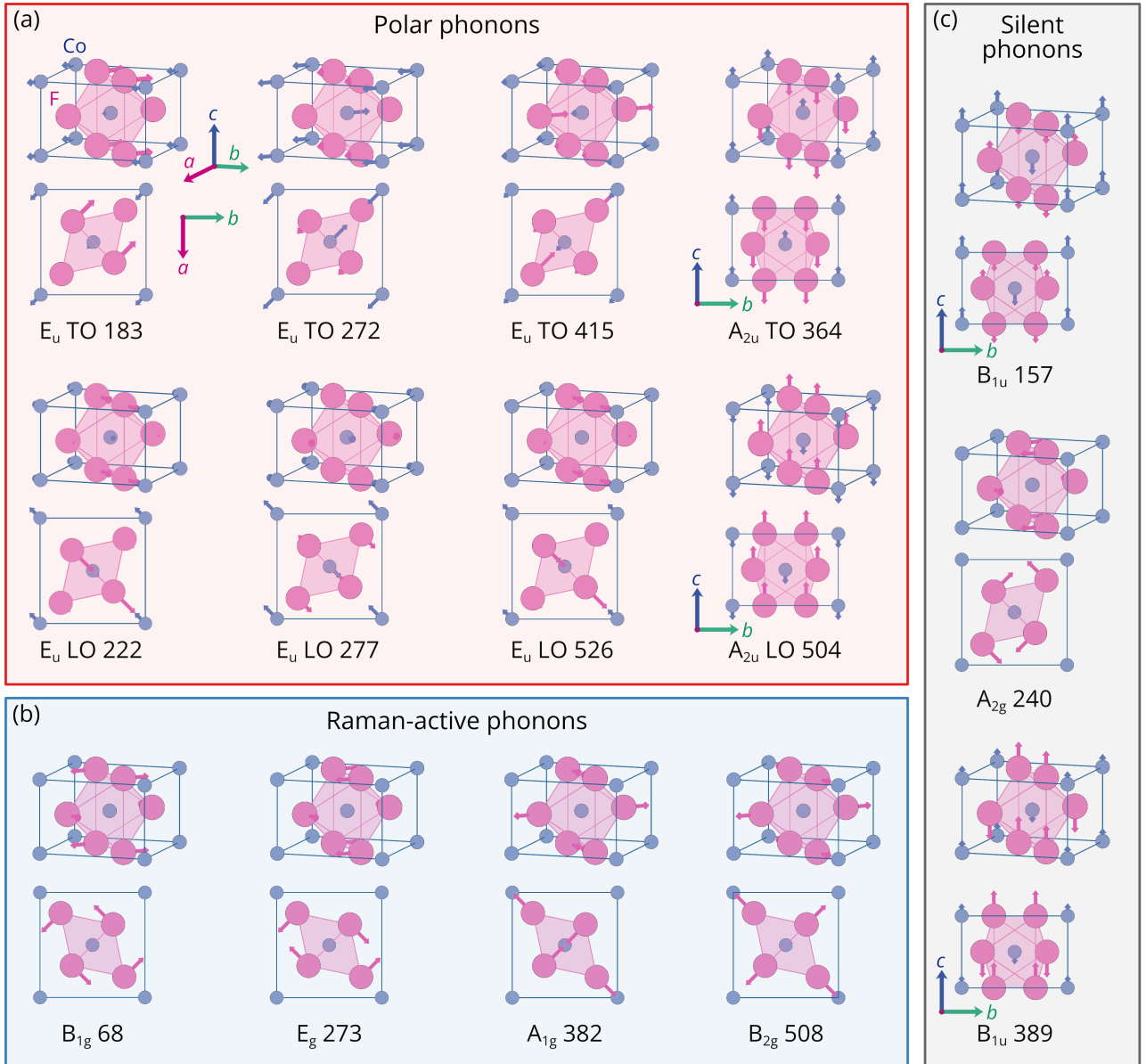


FIG. 7. Sketch of the ion's displacements for (a) polar, (b) Raman-active, and (c) silent optical phonons extracted for CoF_2 in the Brillouin zone center obtained from the DFT calculations. The numbers represent the phonon frequencies in cm^{-1} . The picture was prepared using the VESTA software [123].

shifts $\Delta\omega^{\text{SP}}$ are different in magnitude for TO and LO frequencies of the A_{2u} polar phonons ($\Delta\omega_{\text{TO}}^{\text{SP}} > \Delta\omega_{\text{LO}}^{\text{SP}}$) which proves that the frequency shift is inversely proportional to the phonon frequency [129]. In contrast, for E_u polar phonons, there are slight differences in ion displacements for TO and LO modes [see Fig. 7(a)] due to the slight mode mixing caused by the Coulomb interaction [125; 130; 131].

Aiming to reveal the volume effect on the phonons, we performed lattice dynamics simulations with the unit cell volume change of $\pm 1\%$ as shown in Fig. 6(b). The dispersion curves of phonons qualitatively have the same

behavior in the whole Brillouin zone. Calculated frequencies of phonons at the center of the Brillouin zone as a function of the unit cell volume are shown in Fig. 9. According to Ref. [34], the lattice parameters decrease at cooling in the paramagnetic phase, thereby reducing the unit cell volume in CoF_2 . Figure 9(a) shows that frequencies of not all polar phonons increase at the compression of the unit cell as in our experiment (see Fig. 3). So, the ω_{TO} frequency of the E_u phonon decreases with compression of the unit cell, whereas in our experiment, on the contrary, it increases. Thus, the temperature dependences of not all polar phonons can be explained only

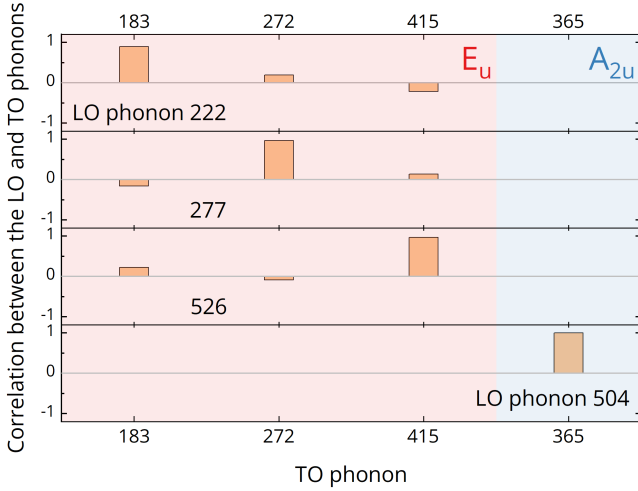


FIG. 8. Correlation between eigendisplacements of LO and TO polar phonons with E_u (red background) and A_{2u} (blue background) symmetry. The latter is extracted according to the DFT calculations at the Γ point of the Brillouin zone and it shows that the “LO-TO” rule is fully satisfied in CoF_2 . The values of the LO phonon frequencies are given in cm^{-1} .

by a harmonic change in the unit cell volume. The frequencies of Raman-active phonons in the calculation, see Fig. 9(b), and experiment [97] behave in the same way at the volume changes. Note that the frequencies of the silent phonons in our calculations change rather weakly when the unit cell volume changes.

According to Ref. [34], the lattice parameters a and b increase, whereas c decreases at cooling below the Néel temperature in the antiferromagnetic phase due to the magnetostriction effect. It can be seen that the change in the volume of the unit cell as a result of magnetostriction cannot explain the sign of frequency shift at the antiferromagnetic ordering since $\Delta\omega^{\text{SP}}$ is negative for A_{2u} phonons. At the same time, the compression of the c axis leads to an increase in its TO and LO frequencies, as shown in Fig. 9(a). The observed phonon frequency shifts at the antiferromagnetic ordering in CoF_2 cannot be explained only due to observed magnetostriction.

We have also estimated the dielectric strengths $\Delta\varepsilon$ and static dielectric permittivity ε_0 using Eq. (8) and phonons frequencies for AFM, FM and NM phases from DFT calculations, which are listed in Table III. There is a good agreement with experimental data from Table I. Moreover, the calculated signs and relative values of the shifts of the dielectric strengths $\Delta\varepsilon^{\text{MD}}$ correspond with the experimental ones for the most polar phonons, as can be seen in Figs. 5(c) and 5(d). The values of the spontaneous magnetodielectric effect $\Delta\varepsilon_0^{\text{MD}}$ obtained from DFT calculations also are in fair agreement with those for low-frequency dielectric permittivity and infrared spectroscopy. Thus, we conclude that the results of our DFT calculations adequately reflect the features of the lattice dynamics related to the antiferromagnetic ordering in CoF_2 .

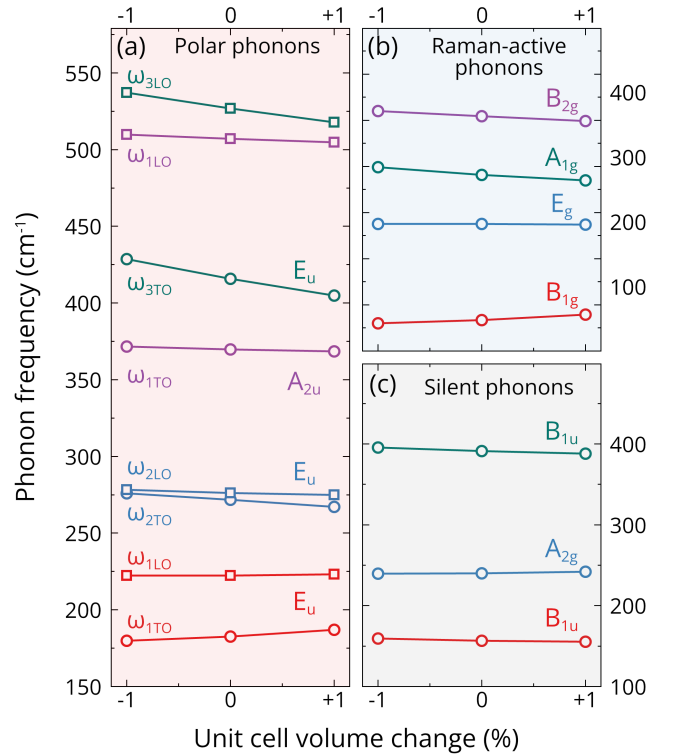


FIG. 9. Calculated frequencies of the (a) polar, (b) Raman-active, and (c) silent optical phonons as a function of the unit cell volume change in the nonmagnetic phase.

D. Magnon-phonon coupling

After observing compelling evidence of spin-phonon coupling, our investigation delves into exploring the effects of phonon displacements on the magnetic properties of CoF_2 . Our approach begins with formulating the effective Heisenberg model, as:

$$H = \sum_{i \neq j} J_{ij} \mathbf{S}_i \mathbf{S}_j. \quad (11)$$

TABLE III. Calculated dielectric strengths $\Delta\varepsilon_j$ of the polar phonons, static ε_0 and high-frequency ε_∞ dielectric permittivities for antiferromagnetic (AFM), ferromagnetic (FM), and nonmagnetic (NM) states along with spontaneous magnetodielectric coupling parameter (MD = AFM - NM) in CoF_2 .

Sym.	Mode j	AFM	FM	NM	MD
E_u	$\Delta\varepsilon_1$	2.23	2.30	2.26	-0.031
	$\Delta\varepsilon_2$	0.103	0.102	0.103	0.001
	$\Delta\varepsilon_3$	1.34	1.32	1.33	0.006
	ε_∞	2.55	2.53	2.54	0.011
	ε_0	6.23	6.25	6.24	-0.013
A_{2u}	$\Delta\varepsilon_1$	2.41	2.23	2.32	0.09
	ε_∞	2.64	2.62	2.63	0.008
	ε_0	5.05	4.85	4.95	0.099

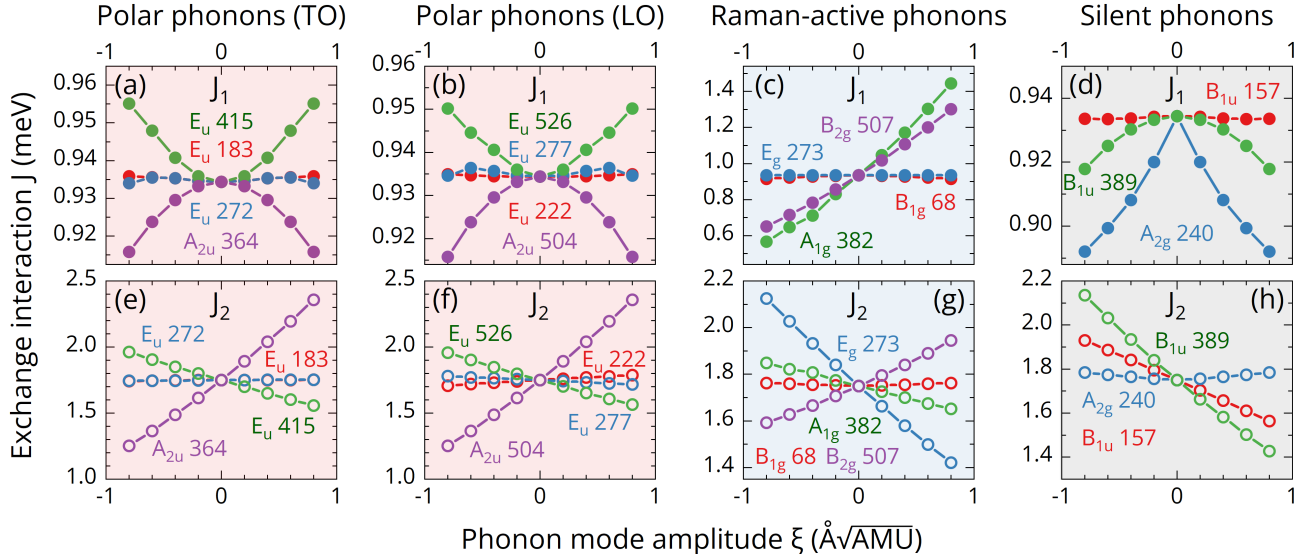


FIG. 10. Computed exchange interactions J_1 and $J_{2,+}$ as a function of the phonon eigendisplacement ξ ($\text{\AA}\sqrt{\text{AMU}}$) for [(a) and (e)] polar TO, [(b) and (f)] polar LO, [(c) and (g)] Raman-active, and [(d) and (h)] silent phonons at the center of the Brillouin zone in CoF_2 , respectively. The numbers represent the phonon frequencies in cm^{-1} .

Here, \mathbf{S}_i (\mathbf{S}_j) represents the unit-length spin operator of the magnetic site i (j), while J_{ij} denotes the isotropic exchange interaction quantifying interactions between magnetic sites i and j . Once the exchange interactions are known, we can obtain the magnon frequencies by diagonalizing the Hesignberg Hamiltonian. Our primary objective centers on scrutinizing the impact of lattice vibrations on the magnon spectra. To achieve this, we compute the perturbations in the exchange interactions elicited by the displacements induced by each distinct phonon mode.

In the case of CoF_2 , the magnetic properties are primarily influenced by the interactions among nearest and next-nearest-neighbors. These interactions are quantified by their respective exchange integrals, denoted as J_1 and J_2 , which are shown in Fig. 1(a). Table IV presents the values of J_1 and J_2 derived from first principles computations for the ground structure of CoF_2 in comparison with experimental data from Refs. [53; 132]. The calculated value of J_2 aligns closely with experimental observations, playing a pivotal role in inducing antiferromagnetic behavior in CoF_2 . In contrast, our computation of J_1 reveals a discrepancy in sign compared to experiments. Notably, this sign mismatch persists across variations in DFT parameters, exchange-correlation functionals, and methodologies employed to determine the exchange constants. Nevertheless, our findings are consistent with those reported for the isostructural antiferromagnet MnF_2 in the existing literature [133]. Despite the ambiguity surrounding the sign of J_1 , we proceed with our analysis based on the consensus regarding the accuracy of the J_2 values.

The exchange interactions in the Heisenberg model are described by fixed values. However, the interaction be-

TABLE IV. Isotropic exchange interactions of CoF_2 .

Method	J_1 (meV)	J_2 (meV)	Reference
Green's function	0.9344	1.7500	This work
Energy mapping	1.034	1.5998	This work
Raman scattering	-0.15	1.6	Ref. [53]
Neutron scattering	-0.207	1.53	Ref. [132]

tween two magnetic sites depends on the distance that separates them. Consequently, the displacements induced by the phonon modes are anticipated to influence the values of J_1 and J_2 . This motivates us to express each exchange constant as

$$J_i^\omega(\xi) = J_i^0 + \alpha_i^\omega \xi + \beta_i^\omega \xi^2 + o(\xi^3), \quad (12)$$

where J_i^0 is the exchange interaction computed by using the equilibrium distances, ξ is the phonon amplitude, and ω labels a particular phonon mode. Furthermore, ξ represents lattice distortions that modify the exchange interactions, which could be induced by strain or optical excitations [134; 135].

The coefficients α and β on the right-hand side of Eq. (12) quantitatively describe the effect of a particular phonon mode on the exchange interactions. To obtain them, we calculate the exchange interactions of the distorted structures given by frozen phonon modulations for different amplitudes and fit the results to Eq. (12). In Fig. 10, we plot the exchange constants as a function of the phonon amplitudes for each phonon mode. The exchange interactions J_1 and J_2 are affected significantly under the influence of the phonon modes. A similar strong modulation of the exchange interaction by phonons has been previously reported in the litera-

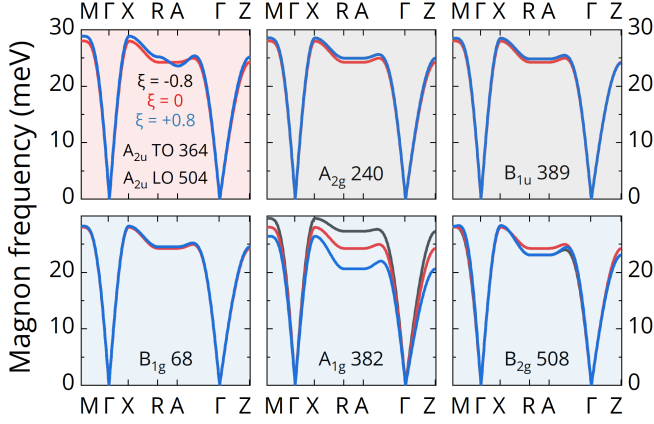


FIG. 11. Computed spin wave dispersion curves along the M- Γ -X-R-A- Γ -Z high-symmetry path of the Brillouin zone for distorted CoF₂ by a frozen polar A_{2u} (red-filled background), silent A_{2g} , B_{1u} (gray-filled background), and Raman-active B_{1g} , A_{1g} , and B_{2g} (blue-filled background) phonons with eigendisplacements $\xi = -0.8, 0$, and $+0.8 \text{ \AA}\sqrt{\text{AMU}}$. The numbers represent the phonon frequencies in cm^{-1} .

ture [136]. On the other hand, the frequency shifts $\Delta\omega^{\text{SP}}$ of phonons at the antiferromagnetic ordering in CoF₂ are rather small, which is indicated by the competing effects of different sign from the dynamical modulation of exchange interactions J_1 and J_2 by phonons due to the coupling with spins. Besides, we see for CoF₂ that the first- and second-order terms of Eq. (12) suffice to account for the exchange interaction variations, and therefore we neglect higher-order terms.

In the unperturbed structure of CoF₂, J_1 and J_2 have

TABLE V. Calculated magnon-phonon coupling coefficients α_i ($\text{meV AMU}^{-\frac{1}{2}} \text{ \AA}^{-1}$) and β_i ($\text{meV AMU}^{-1} \text{ \AA}^{-2}$) of the nearest J_1 and next-nearest-neighbor $J_{2,+}$ exchange interactions as a function of the phonon amplitude. AMU is the atomic mass unit.

Act.	Sym.	Phonon	α_1	β_1	α_2	β_2
IR	E_u	$\omega_{1\text{TO}}$	0.000	0.002	0.005	0.004
		$\omega_{1\text{LO}}$	0.000	0.002	-0.049	-0.004
		$\omega_{2\text{TO}}$	0.000	-0.001	0.006	-0.001
		$\omega_{2\text{LO}}$	0.000	-0.000	0.039	-0.002
		$\omega_{3\text{TO}}$	0.000	0.032	-0.252	0.017
		$\omega_{3\text{LO}}$	0.000	0.024	-0.245	0.020
R	A_{2u}	$\omega_{1\text{TO}}$	0.000	-0.029	0.691	0.085
		$\omega_{1\text{LO}}$	0.000	-0.029	0.691	0.085
	B_{1g}	0.000	-0.028	0.000	0.018	
	E_g	0.000	0.001	-0.440	0.035	
	A_{1g}	0.551	0.118	-0.125	-0.002	
S	B_{2g}	0.406	0.065	0.219	-0.030	
	B_{1u}	0.000	-0.001	-0.229	-0.004	
	A_{2g}	0.000	-0.053	0.000	0.050	
	B_{1u}	0.000	-0.026	-0.442	-0.050	

the same value for all possible nearest and next-nearest-neighbor pairs of the Co ions, respectively. This is, generally, not true for the displaced structures since the distances and thus the interactions between neighbors can be different for equivalent pairs. In our case, we see that $J_1^\omega(\xi)$ is the same for different nearest neighbor pairs (4 in total). This is because the phonons at the Brillouin zone center only produce intra-cell displacements, whereas J_1 corresponds to an inter-cell interaction. In contrast, the next-nearest-neighbor pairs (16 in total) are split into two equal groups characterized by the expression:

$$J_{2,\pm}^\omega(\xi) = J_2^0 \pm \alpha_2^\omega \xi + \beta_2^\omega \xi^2 + o(\xi^3), \quad (13)$$

where $J_{2,+}$ ($J_{2,-}$) describes the interaction between two neighbors when their distance is increased (reduced) during a positive amplitude modulation. These two groups of interactions appear for every phonon mode except for B_{1g} , A_{1g} , and A_{2g} . In Table V, we show the coupling coefficients for the nearest J_1 and next-nearest interactions $J_{2,+}$.

The preceding discussion underscores the anticipated dependence of magnon frequencies on phonon modulations. To scrutinize this relationship, we calculate the magnon spectra corresponding to the distorted structures induced by each phonon mode. The most representative outcomes of these analyses are depicted in Fig. 11. Note that, in general, the magnon (M) frequency at the Brillouin zone center $\omega_M = \gamma\sqrt{2H_A H_E}$, where γ is a gyromagnetic ratio, H_A is a magnetic anisotropy field, and H_E is an exchange field [137]. Since accounting for magnetic anisotropy is a challenging task, we did not take it into account in the calculations and assumed that $H_A = 0$. Thus, the magnon frequency at the Γ point in our calculations is 0 meV whereas in our experiment it was 4.6 meV (37 cm^{-1}). At the Brillouin zone boundaries, the magnon frequencies are determined only by the exchange interactions. The two-magnon (2M) mode frequency 14.2 meV (115 cm^{-1}) allow us to estimate the magnon frequency at the Brillouin zone boundaries as 7.1 meV. This exceeds the calculated values of 24–28 meV (see Fig. 11), which we attribute to a significant discrepancy in the value of the exchange interaction J_1 between experiment and theory. Other studies analyze the magnon-phonon hybridization based on the overlap of the magnon and phonon spectra [138; 139]. In contrast, this study only considers the modulations of the magnon spectra coming from phonons at the center of the Brillouin zone and does not discuss of any avoided crossing between phonons and magnons [42].

For most phonons slight variations in the magnon spectra as a result of modulation are observed as shown, for example, for the Raman-active B_{1g} phonon in Fig. 11. Intriguingly, we observe that the most significant alterations in magnon frequencies stem from the A_{1g} mode despite it not possessing the most significant coupling coefficients as can be seen in Fig. 11 and Table V, respectively. Conversely, modes characterized by more significant coupling coefficients, such as A_{2u} or E_g , exhibit marginal

deviations compared to the ground structure. This phenomenon can be elucidated by examining how the Heisenberg Hamiltonian evolves under a given phonon distortion. Specifically, for a designated phonon amplitude ξ , we construct a modified Hamiltonian considering the interactions among the 4 and 16 nearest and next-nearest-neighbors as follows:

$$\begin{aligned}
 H^\omega(\xi) &= -2J_1^\omega(\xi) (\mathbf{S}_1^2 + \mathbf{S}_2^2) \\
 &\quad - 8J_{2,-}^\omega(\xi) \mathbf{S}_1 \mathbf{S}_2 - 8J_{2,+}^\omega(\xi) \mathbf{S}_1 \mathbf{S}_2 \\
 &= -2J_1^\omega(\xi) (\mathbf{S}_1^2 + \mathbf{S}_2^2) - 8 [J_{2,-}^\omega(\xi) + J_{2,+}^\omega(\xi)] \mathbf{S}_1 \mathbf{S}_2 \\
 &= -2J_1^\omega(\xi) (\mathbf{S}_1^2 + \mathbf{S}_2^2) - 8 (J_2^0 + 2\beta_2^\omega \xi^2) \mathbf{S}_1 \mathbf{S}_2.
 \end{aligned} \tag{14}$$

The Hamiltonian's actual form (14) reveals that the linear coefficient, α_2^ω , does not affect the magnon dispersion energies, as two types of interactions, $J_{2,-}^\omega$ and $J_{2,+}^\omega$, emerge. Consequently, in CoF₂, next-nearest-neighbor interactions J_2 contribute to magnon-phonon coupling only if they respond quadratically to lattice distortions. This clarifies why many phonon modes do not couple to magnetic response, as they primarily induce linear changes in J_2 (i.e., $\beta_2^\omega \approx 0$). Only distortions from A_{1g} and B_{2g} modes notably modify J_1 , thereby influencing the magnon spectra as can be seen in Table V. Therefore, even if a phonon mode can individually alter the exchange interactions, it may not measurably affect the magnetic properties. It should be mentioned that it has been shown experimentally that magnon is strongly coupled to the Raman-active B_{1g} phonon in CoF₂ [41]. But according to our calculation results the effect of influence of the B_{1g} mode to the magnon spectrum is rather small as can be seen in Fig. 11. The discrepancy arises because the experiment focused on studying the magnon at the center of the Brillouin zone, while our calculations did not account for magnetic anisotropy, which is critical for capturing the coupling between magnons and phonons at the Γ point.

IV. CONCLUSIONS AND GENERAL REMARKS

In summary, we have studied in detail the polar phonons at the Γ point of the Brillouin zone in the rutile antiferromagnet CoF₂ in a wide temperature range, including the antiferromagnetic phase transition by far-infrared and dielectric spectroscopic techniques. We have experimentally observed that all polar phonons' TO and LO frequencies shift at the antiferromagnetic phase transition. Moreover, our measurements have shown that the low-frequency dielectric permittivity also shifts at T_N due to the spontaneous magnetodielectric effect. Still, the signs of these changes are opposite for the a and c axes. The combined analysis of these experimental results showed that the observed spontaneous magnetodielectric effect is mostly caused by changes in the frequencies of polar phonons at antiferromagnetic ordering.

Based on our first-principles calculations, we have found that observed shifts of frequencies of all polar phonons are fairly reproduced with antiferromagnetic ordering and unrelated to the unit cell changes due to the magnetostriction in CoF₂. Thus, according to the calculations, the observed frequency changes of polar phonons and the low-frequency dielectric permittivity results due to spin-phonon coupling and spontaneous magnetodielectric effect are related to the dynamic modulation of the exchange interaction by phonons. In addition, we have observed magnetic excitations in the infrared spectra and identified their magnetodipole origin. First-principles calculations corroborate these observations, emphasizing the coupling between polar phonons and magnons through the dynamic modulation of the exchange interactions.

Notably, the most pronounced impact on the nearest-neighbor coupling J_1 is discernible in the Raman phonon A_{1g} mode, evident across both linear and quadratic regimes, albeit to a lesser extent on E_g modes. While certain phonons may lack linear contributions to J_1 , they exhibit discernible quadratic contributions, which define the strength of the phonon-magnon coupling [140]. Conversely, concerning the next-nearest-neighbor coupling J_2 , myriad infrared, silent, and Raman modes exhibit linear coupling, with the quadratic contributions typically on par with or subordinate to those observed in the J_1 scenario. Regardless, significant phonon coupling in magnon spectra manifests predominantly when the quadratic term attains substantial magnitude, notably exemplified in the A_{1g} mode and, to a lesser degree, in the B_{2g} mode. Intriguingly, specific infrared and silent modes exhibit more significant linear coupling than their Raman counterparts.

We believe our results will stimulate further experimental and theoretical studies of nonlinear phononics in the antiferromagnet CoF₂, in which a nontrivial nonlinear coupling was observed between polar, Raman-active phonons and magnons. The other attractive materials based on the $3d^7$ Co²⁺ ions with the unquenched orbital angular momentum and strong spin-orbit effects are insulating honeycomb magnets, e.g., Na₂Co₂TeO₆ and Na₃Co₂SbO₆, which are of considerable scientific interest at the present time as a potential Kitaev system with nontrivial spin-phonon couplings which has yet to be revealed [141–146].

ACKNOWLEDGMENTS

We are grateful to V.A. Chernyshev for fruitful scientific discussion. We thank D.A. Andronikova and M.P. Scheglov for the help with the x-ray orientation of single crystal. The single crystal grown by S.V. Petrov was used in experiments. This work was supported by the Russian Science Foundation under grant no. 22-72-00025, <https://rscf.ru/en/project/22-72-00025/>. R.M.D. acknowledges the support of the Ministry of Science and

Higher Education of the Russian Federation (FSWR-2024-0003). N.N.N. and K.N.B. acknowledge support by the research Project No. FFUU-2022-0003 of the Institute of Spectroscopy of the Russian Academy of Sciences. Some calculations included in this article were carried out using the GridUIS-2 experimental testbed. The latter was developed under the Universidad Industrial de Santander (SC3-UIS) High Performance and Scientific Computing Centre with support from UIS Vicerrectoría de Investigación y Extensión (VIE-UIS) and several UIS research groups. A.C.G.C. acknowledge grant No. 202303059C entitled “Optimización de las Propiedades Termoeléctricas Mediante Tensión Biaxial

en la Familia de Materiales $\text{Bi}_4\text{O}_4\text{SeX}_2$ ($X = \text{Cl}, \text{Br}, \text{I}$) Desde Primeros Principios” supported by the LNS - BUAP. The group at West Virginia University thanks the Pittsburgh Supercomputer Center (Bridges2) and San Diego Supercomputer Center (Expanse) through allocation DMR140031 from the Advanced Cyberinfrastructure Coordination Ecosystem: Services & Support (ACCESS) program, which is supported by National Science Foundation grants #2138259, #2138286, #2138307, #2137603, and #2138296. They also recognize the support of West Virginia Research under the call Research Challenge Grand Program 2022 and NASA EPSCoR Award 80NSSC22M0173.

-
- [1] T. Jungwirth, X. Marti, P. Wadley, and J. Wunderlich, Antiferromagnetic spintronics, *Nat. Nanotechnol.* **11**, 231 (2016).
- [2] V. Baltz, A. Manchon, M. Tsoi, T. Moriyama, T. Ono, and Y. Tserkovnyak, Antiferromagnetic spintronics, *Rev. Mod. Phys.* **90**, 015005 (2018).
- [3] T. Jungwirth, J. Sinova, A. Manchon, X. Marti, J. Wunderlich, and C. Felser, The multiple directions of antiferromagnetic spintronics, *Nat. Phys.* **14**, 200 (2018).
- [4] P. Nêmec, M. Fiebig, T. Kampfrath, and A. V. Kimel, Antiferromagnetic opto-spintronics, *Nat. Phys.* **14**, 229 (2018).
- [5] Z. Liu, Z. Feng, H. Yan, X. Wang, X. Zhou, P. Qin, H. Guo, R. Yu, and C. Jiang, Antiferromagnetic piezospintronics, *Adv. Electron. Mater.* **5**, 1900176 (2019).
- [6] S. Fukami, V. O. Lorenz, and O. Gomonay, Antiferromagnetic spintronics, *J. Appl. Phys.* **128**, 070401 (2020).
- [7] A. Brataas, B. van Wees, O. Klein, G. de Loubens, and M. Viret, Spin Insulatronics, *Phys. Rep.* **885**, 1 (2020).
- [8] L. Flórez-Gómez, W. Ibarra-Hernández, and A. C. Garcia-Castro, Lattice dynamics and spin-phonon coupling in the noncollinear antiferromagnetic antiperovskite Mn_3NiN , *J. Magn. Magn. Mater.* **562**, 169813 (2022).
- [9] D. Xiong, Y. Jiang, K. Shi, A. Du, Y. Yao, Z. Guo, D. Zhu, K. Cao, S. Peng, W. Cai, *et al.*, Antiferromagnetic spintronics: An overview and outlook, *Fundam. Res.* **2**, 522 (2022).
- [10] J. Han, R. Cheng, L. Liu, H. Ohno, and S. Fukami, Coherent antiferromagnetic spintronics, *Nat. Mater.* **22**, 684 (2023).
- [11] H. Meer, O. Gomonay, A. Wittmann, and M. Kläui, Antiferromagnetic insulatronics: Spintronics in insulating 3d metal oxides with antiferromagnetic coupling, *Appl. Phys. Lett.* **122**, 10.1063/5.0135079 (2023).
- [12] T. F. Nova, A. Cartella, A. Cantaluppi, M. Först, D. Bossini, R. V. Mikhaylovskiy, A. V. Kimel, R. Merlin, and A. Cavalleri, An effective magnetic field from optically driven phonons, *Nat. Phys.* **13**, 132 (2017).
- [13] S. Streib, N. Vidal-Silva, K. Shen, and G. E. W. Bauer, Magnon-phonon interactions in magnetic insulators, *Phys. Rev. B* **99**, 184442 (2019).
- [14] D. M. Juraschek, P. Narang, and N. A. Spaldin, Phonomagnetic analogs to opto-magnetic effects, *Phys. Rev. Research* **2**, 043035 (2020).
- [15] D. M. Juraschek, D. S. Wang, and P. Narang, Sum-frequency excitation of coherent magnons, *Phys. Rev. B* **103**, 094407 (2021).
- [16] A. Stupakiewicz, C. Davies, K. Szerenos, D. Afanasiev, K. Rabinovich, A. Boris, A. Caviglia, A. Kimel, and A. Kirilyuk, Ultrafast phononic switching of magnetization, *Nat. Phys.* **17**, 489 (2021).
- [17] D. Afanasiev, J. Hortensius, B. Ivanov, A. Sasani, E. Bousquet, Y. Blanter, R. Mikhaylovskiy, A. Kimel, and A. Caviglia, Ultrafast control of magnetic interactions via light-driven phonons, *Nat. Mater.* **20**, 607 (2021).
- [18] A. S. Disa, T. F. Nova, and A. Cavalleri, Engineering crystal structures with light, *Nat. Phys.* **17**, 1087 (2021).
- [19] H. Ueda, R. Mankowsky, E. Paris, M. Sander, Y. Deng, B. Liu, L. Leroy, A. Nag, E. Skoropata, C. Wang, V. Ukleev, G. S. Perren, J. Dössegger, S. Gurung, C. Svetina, E. Abreu, M. Savoini, T. Kimura, L. Patthey, E. Razzoli, H. T. Lemke, S. L. Johnson, and U. Staub, Non-equilibrium dynamics of spin-lattice coupling, *Nat. Commun.* **14**, 7778 (2023).
- [20] C. Davies, F. G. N. Fennema, A. Tsukamoto, I. Razdolski, A. V. Kimel, and A. Kirilyuk, Phononic switching of magnetization by the ultrafast Barnett effect, *Nature* **628**, 540 (2024).
- [21] M. Basini, M. Pancaldi, B. Wehinger, M. Udina, V. Unikandanunni, T. Tadano, M. C. Hoffmann, A. V. Balatsky, and S. Bonetti, Terahertz electric-field-driven dynamical multiferroicity in SrTiO_3 , *Nature* **628**, 534 (2024).
- [22] M. Gu, Y. H. Bai, G. P. Zhang, and T. F. George, Spin-phonon dispersion in magnetic materials, *J. Phys. Condens. Matter* **34**, 375802 (2022).
- [23] Y. Guo, H. Liu, O. Janson, I. C. Fulga, J. van den Brink, and J. I. Facio, Spin-split collinear antiferromagnets: a large-scale ab-initio study, *Mater. Today Phys.* **32**, 100991 (2023).
- [24] S. M. Wu, W. Zhang, A. KC, P. Borisov, J. E. Pearson, J. S. Jiang, D. Lederman, A. Hoffmann, and A. Bhatlacharya, Antiferromagnetic spin seebeck effect, *Phys. Rev. Lett.* **116**, 097204 (2016).

- [25] J. Li, Z. Shi, V. H. Ortiz, M. Aldosary, C. Chen, V. Aji, P. Wei, and J. Shi, Spin Seebeck Effect from Antiferromagnetic Magnons and Critical Spin Fluctuations in Epitaxial FeF₂ films, *Phys. Rev. Lett.* **122**, 217204 (2019).
- [26] P. Vaidya, S. A. Morley, J. van Tol, Y. Liu, R. Cheng, A. Brataas, D. Lederman, and E. Del Barco, Subterahertz spin pumping from an insulating antiferromagnet, *Science* **368**, 160 (2020).
- [27] D. J. Lockwood and M. G. Cottam, The spin-phonon interaction in FeF₂ and MnF₂ studied by Raman spectroscopy, *J. Appl. Phys.* **64**, 5876 (1988).
- [28] R. Schleck, Y. Nahas, R. P. S. M. Lobo, J. Varignon, M. B. Lepetit, C. S. Nelson, and R. L. Moreira, Elastic and magnetic effects on the infrared phonon spectra of MnF₂, *Phys. Rev. B* **82**, 054412 (2010).
- [29] M. S. Seehra and R. E. Helmick, Anomalous changes in the dielectric constants of MnF₂ near its Néel temperature, *J. Appl. Phys.* **55**, 2330 (1984).
- [30] M. S. Seehra, R. E. Helmick, and G. Srinivasan, Effect of temperature and antiferromagnetic ordering on the dielectric constants of MnO and MnF₂, *J. Phys. C: Solid State Phys.* **19**, 1627 (1986).
- [31] T. Moriya, K. Motizuki, J. Kanamori, and T. Nagamiya, On the Magnetic Anisotropy of FeF₂ and CoF₂, *J. Phys. Soc. Jpn.* **11**, 211 (1956).
- [32] C. A. Corrêa and K. Vyborny, Electronic structure and magnetic anisotropies of antiferromagnetic transition-metal difluorides, *Phys. Rev. B* **97**, 235111 (2018).
- [33] W. Jauch, M. Reehuis, and A. J. Schultz, γ -ray and neutron diffraction studies of CoF₂: magnetostriction, electron density and magnetic moments, *Acta Cryst.* **A60**, 51 (2004).
- [34] T. Chatterji, B. Ouladdiaf, and T. C. Hansen, The magnetoelastic effect in CoF₂ investigated by means of neutron powder diffraction, *J. Phys. Condens. Matter* **22**, 096001 (2010).
- [35] A. Borovik-Romanov, Piezomagnetism in the antiferromagnetic fluorides of cobalt and manganese, *Sov. Phys. JETP* **11**, 786 (1960).
- [36] T. Moriya, Piezomagnetism in CoF₂, *J. Phys. Chem. Solids* **11**, 73 (1959).
- [37] T. G. Phillips, R. L. Townsend, and R. L. White, Piezomagnetism of CoF₂ and α -Fe₂O₃ from electron-paramagnetic-resonance pressure experiments, *Phys. Rev. Lett.* **18**, 646 (1967).
- [38] A. S. Disa, M. Fechner, T. F. Nova, B. Liu, M. Först, D. Prabhakaran, P. G. Radaelli, and A. Cavalleri, Polarizing an antiferromagnet by optical engineering of the crystal field, *Nat. Phys.* (2020).
- [39] F. Formisano, R. M. Dubrovina, R. V. Pisarev, A. M. Kalashnikova, and A. V. Kimel, Laser-induced THz magnetism of antiferromagnetic CoF₂, *J. Phys. Condens. Matter* **34**, 225801 (2022).
- [40] F. Formisano, R. M. Dubrovina, R. V. Pisarev, A. K. Zvezdin, A. M. Kalashnikova, and A. V. Kimel, Laser-induced THz piezomagnetism and lattice dynamics of antiferromagnets MnF₂ and CoF₂, *Ann. Phys.* , 169041 (2022).
- [41] E. A. Mashkovich, K. A. Grishunin, R. M. Dubrovina, A. K. Zvezdin, R. V. Pisarev, and A. V. Kimel, Terahertz light-driven coupling of antiferromagnetic spins to lattice, *Science* **374**, 1608 (2021).
- [42] T. W. Metzger, K. A. Grishunin, C. Reinhofer, R. M. Dubrovina, A. Arshad, I. Ilyakov, T. V. de Oliveira, A. Ponomaryov, J.-C. Deinert, S. Kovalev, R. V. Pisarev, M. I. Katsnelson, B. A. Ivanov, P. H. van Loosdrecht, A. V. Kimel, and E. A. Mashkovich, Impulsive fermi magnon-phonon resonance in antiferromagnetic CoF₂, arXiv preprint arXiv:2308.01052 [10.48550/arXiv.2308.01052](https://arxiv.org/abs/2308.01052) (2023).
- [43] V. Ozhogin, The antiferromagnets CoCO₃, CoF₂, and FeCO₃ in strong fields, *Soviet Physics JETP-USSR* **18**, 1156 (1964).
- [44] V. I. Ozhogin, On the Behavior of CoF₂ in a High Magnetic Field Normal to the *c* Axis, *J. Appl. Phys.* **39**, 1029 (1968).
- [45] Y. M. Gufan, K. Kocharyan, A. Prokhorov, and E. Rudashevskii, Dependence of the resonant frequencies of antiferromagnets on the magnetic field, and antiferromagnetic resonance in CoF₂, *JETP* **66**, 1155 (1974).
- [46] N. F. Kharchenko, V. V. Eremenko, and L. Belyi, Magneto-optical investigation of the noncollinear state induced in antiferromagnetic cobalt fluoride by a longitudinal magnetic field, *Sov. Phys. JETP* **55**, 490 (1982).
- [47] K. G. Gurtovoi, A. S. Lagutin, and V. I. Ozhogin, Noncollinear magnetic phases in a strongly anisotropic antiferromagnet CoF₂ with large dzyaloshinskii interaction, *Sov. Phys. JETP* **26**, 1122 (1982).
- [48] R. M. Macfarlane, Raman Light Scattering from Excitons and Magnons in Cobalt Fluoride, *Phys. Rev. Lett.* **25**, 1454 (1970).
- [49] A. Ishikawa and T. Moriya, Magnons, Excitons and Light Scattering in Antiferromagnetic CoF₂, *J. Phys. Soc. Jpn.* **30**, 117 (1971).
- [50] E. Meloche, M. G. Cottam, and D. J. Lockwood, One-magnon and exciton inelastic light scattering in the antiferromagnet CoF₂, *Low Temp. Phys.* **40**, 134 (2014).
- [51] J. Cipriani, S. Racine, and R. Dupeyrat, Raman scattering by two-magnon excitations in CoF₂, *Phys. Lett. A* **34**, 187 (1971).
- [52] C. R. Natoli and J. Ranninger, Two-magnon neutron scattering in CoF₂, *J. Phys. C: Solid State Phys.* **6**, 370 (1973).
- [53] E. Meloche, M. G. Cottam, and D. J. Lockwood, Two-magnon inelastic light scattering in the antiferromagnets CoF₂ and NiF₂: Experiment and theory, *Phys. Rev. B* **76**, 104406 (2007).
- [54] R. Cowley, W. Buyers, P. Martel, and R. Stevenson, Magnetic excitations and magnetic critical scattering in cobalt fluoride, *J. Phys. C: Solid State Phys.* **6**, 2997 (1973).
- [55] R. M. Macfarlane and S. Ushioda, Light scattering from phonons in CoF₂, *Solid State Commun.* **8**, 1081 (1970).
- [56] A. S. Barker Jr and J. A. Ditzenberger, Infrared lattice vibrations in CoF₂, *Solid State Commun.* **3**, 131 (1965).
- [57] M. Balkanski, P. Moch, and G. Parisot, Infrared lattice-vibration spectra in NiF₂, CoF₂, and FeF₂, *J. Chem. Phys.* **44**, 940 (1966).
- [58] K. M. Häussler, Infrared spectra of magnetic excitations in CoF₂, *Phys. Status Solidi B* **105**, K81 (1981).
- [59] J. W. Stout and S. A. Reed, The crystal structure of MnF₂, FeF₂, CoF₂, NiF₂ and ZnF₂, *J. Am. Chem. Soc.* **76**, 5279 (1954).
- [60] M. M. R. Costa, J. A. Paixao, M. J. M. De Almeida, and L. C. R. Andrade, Charge densities of two rutile struc-

- tures: NiF₂ and CoF₂, *Acta Cryst.* **B49**, 591 (1993).
- [61] R. I. Thomson, T. Chatterji, and M. A. Carpenter, CoF₂: a model system for magnetoelastic coupling and elastic softening mechanisms associated with paramagnetic ↔ antiferromagnetic phase transitions, *J. Phys. Condens. Matter* **26**, 146001 (2014).
- [62] J. W. Stout and L. M. Matarrese, Magnetic Anisotropy of the Iron-Group Fluorides, *Rev. Mod. Phys.* **25**, 338 (1953).
- [63] R. A. Erickson, Neutron Diffraction Studies of Antiferromagnetism in Manganous Fluoride and Some Isomorphous Compounds, *Phys. Rev.* **90**, 779 (1953).
- [64] J. Strempler, U. Rütt, S. P. Bayrakci, T. Brückel, and W. Jauch, Magnetic properties of transition metal fluorides MF₂ (M = Mn, Fe, Co, Ni) via high-energy photon diffraction, *Phys. Rev. B* **69**, 014417 (2004).
- [65] V. V. Ereminenko, V. M. Naumenko, S. V. Petrov, and V. V. Pishko, Rearrangement of the spectrum of magnetic excitations of antiferromagnetic CoF₂ with low-concentration MnF₂ impurity, *JETP* **55**, 481 (1982).
- [66] P. Hohenberg and W. Kohn, Inhomogeneous Electron Gas, *Phys. Rev.* **136**, B864 (1964).
- [67] W. Kohn and L. J. Sham, Self-Consistent Equations Including Exchange and Correlation Effects, *Phys. Rev.* **140**, A1133 (1965).
- [68] P. E. Blöchl, Projector augmented-wave method, *Phys. Rev. B* **50**, 17953 (1994).
- [69] G. Kresse and J. Furthmüller, Efficient iterative schemes for *ab initio* total-energy calculations using a plane-wave basis set, *Phys. Rev. B* **54**, 11169 (1996).
- [70] G. Kresse and D. Joubert, From ultrasoft pseudopotentials to the projector augmented-wave method, *Phys. Rev. B* **59**, 1999 (1999).
- [71] H. J. Monkhorst and J. D. Pack, Special points for Brillouin-zone integrations, *Phys. Rev. B* **13**, 5188 (1976).
- [72] J. P. Perdew, A. Ruzsinszky, G. I. Csonka, O. A. Vydrov, G. E. Scuseria, L. A. Constantin, X. Zhou, and K. Burke, Restoring the Density-Gradient Expansion for Exchange in Solids and Surfaces, *Phys. Rev. Lett.* **100**, 136406 (2008).
- [73] S. L. Dudarev, G. A. Botton, S. Y. Savrasov, C. J. Humphreys, and A. P. Sutton, Electron-energy-loss spectra and the structural stability of nickel oxide: An LSDA+U study, *Phys. Rev. B* **57**, 1505 (1998).
- [74] E. Bousquet and N. Spaldin, *J* dependence in the LSDA + *U* treatment of noncollinear magnets, *Phys. Rev. B* **82**, 220402 (2010).
- [75] X. Gonze and C. Lee, Dynamical matrices, Born effective charges, dielectric permittivity tensors, and interatomic force constants from density-functional perturbation theory, *Phys. Rev. B* **55**, 10355 (1997).
- [76] A. Togo and I. Tanaka, First principles phonon calculations in materials science, *Scr. Mater.* **108**, 1 (2015).
- [77] Y. Wang, J. J. Wang, W. Y. Wang, Z. G. Mei, S. L. Shang, L. Q. Chen, and Z. K. Liu, A mixed-space approach to first-principles calculations of phonon frequencies for polar materials, *J. Phys. Condens. Matter* **22**, 202201 (2010).
- [78] ladyteam, *LAttice DYNamic tools*.
- [79] A. I. Liechtenstein, M. I. Katsnelson, V. P. Antropov, and V. A. Gubanov, Local spin density functional approach to the theory of exchange interactions in ferromagnetic metals and alloys, *J. Magn. Magn. Mater.* **67**, 65 (1987).
- [80] X. He, N. Helbig, M. J. Verstraete, and E. Bousquet, TB2J: A python package for computing magnetic interaction parameters, *Comput. Phys. Commun.* **264**, 107938 (2021).
- [81] A. Tellez-Mora, X. He, E. Bousquet, L. Wirtz, and A. H. Romero, Systematic determination of a material's magnetic ground state from first principles, *npj Comput. Mater.* **10**, 20 (2024).
- [82] J. M. Soler, E. Artacho, J. D. Gale, A. García, J. Junquera, P. Ordejón, and D. Sánchez-Portal, The SIESTA method for *ab initio* order-N materials simulation, *J. Phys. Condens. Matter* **14**, 2745 (2002).
- [83] S. Toth and B. Lake, Linear spin wave theory for single-q incommensurate magnetic structures, *J. Phys.: Condens. Matter* **27**, 166002 (2015).
- [84] E. Kroumova, M. I. Aroyo, J. M. Perez-Mato, A. Kirov, C. Capillas, S. Ivantchev, and H. Wondratschek, Bilbao Crystallographic Server: Useful Databases and Tools for Phase-Transition Studies, *Phase Transit.* **76**, 155 (2003).
- [85] M. Born and E. Wolf, *Principles of Optics: Electromagnetic Theory of Propagation, Interference and Diffraction of Light* (Elsevier, 2013).
- [86] F. Gervais and B. Piriou, Anharmonicity in several-polar-mode crystals: adjusting phonon self-energy of LO and TO modes in Al₂O₃ and TiO₂ to fit infrared reflectivity, *J. Phys. C: Solid State Phys.* **7**, 2374 (1974).
- [87] C. Benoit and J. Giordano, Dynamical properties of crystals of MgF₂, ZnF₂ and FeF₂. II. Lattice dynamics and infrared spectra, *Journal of Physics C: Solid State Physics* **21**, 5209 (1988).
- [88] A. S. Barker, Transverse and Longitudinal Optic Mode Study in MgF₂ and ZnF₂, *Phys. Rev.* **136**, A1290 (1964).
- [89] J. Hemberger, T. Rudolf, H.-A. Krug von Nidda, F. Mayr, A. Pimenov, V. Tsurkan, and A. Loidl, Spin-Driven Phonon Splitting in Bond-Frustrated ZnCr₂S₄, *Phys. Rev. Lett.* **97**, 087204 (2006).
- [90] T. Rudolf, C. Kant, F. Mayr, and A. Loidl, Magnetic-order induced phonon splitting in MnO from far-infrared spectroscopy, *Phys. Rev. B* **77**, 024421 (2008).
- [91] C. Kant, J. Deisenhofer, T. Rudolf, F. Mayr, F. Schrettle, A. Loidl, V. Gnezdilov, D. Wulferding, P. Lemmens, and V. Tsurkan, Optical phonons, spin correlations, and spin-phonon coupling in the frustrated pyrochlore magnets CdCr₂O₄ and ZnCr₂O₄, *Phys. Rev. B* **80**, 214417 (2009).
- [92] C. Kant, M. Schmidt, Z. Wang, F. Mayr, V. Tsurkan, J. Deisenhofer, and A. Loidl, Universal Exchange-Driven Phonon Splitting in Antiferromagnets, *Phys. Rev. Lett.* **108**, 177203 (2012).
- [93] B. Wei, Q. Sun, C. Li, and J. Hong, Phonon anharmonicity: a pertinent review of recent progress and perspective, *Sci. China Phys. Mech. Astron.* **64**, 117001 (2021).
- [94] M. Born and K. Huang, *Dynamical Theory of Crystal Lattices* (Clarendon press, Oxford, 1954).
- [95] M. Balkanski, R. F. Wallis, and E. Haro, Anharmonic effects in light scattering due to optical phonons in silicon, *Phys. Rev. B* **28**, 1928 (1983).
- [96] T. Lan, X. Tang, and B. Fultz, Phonon anharmonicity of rutile TiO₂ studied by Raman spectrometry and molecular dynamics simulations, *Phys. Rev. B* **85**, 094305

- (2012).
- [97] M. G. Cottam and D. J. Lockwood, Spin-phonon interaction in transition-metal difluoride antiferromagnets: Theory and experiment, *Low Temp. Phys.* **45**, 78 (2019).
- [98] M. I. Darby, Tables of the Brillouin function and of the related function for the spontaneous magnetization, *Br. J. Appl. Phys.* **18**, 1415 (1967).
- [99] T. Moriya, Far Infrared Absorption by Two Magnon Excitations in Antiferromagnets, *J. Phys. Soc. Jpn.* **21**, 926 (1966).
- [100] P. Martel, R. A. Cowley, and R. W. H. Stevenson, Experimental studies of the magnetic and phonon excitations in cobalt fluoride, *Can. J. Phys.* **46**, 1355 (1968).
- [101] S. J. Allen and H. J. Guggenheim, Magnetic Excitations in Antiferromagnetic CoF_2 . I. Spin-Optical-Phonon Interaction, *Phys. Rev. B* **4**, 937 (1971).
- [102] S. J. Allen and H. J. Guggenheim, Magnetic Excitations in Antiferromagnetic CoF_2 . II. Uniform Magnetic Excitations near $t = 0^\circ \text{K}$, *Phys. Rev. B* **4**, 950 (1971).
- [103] R. Newman and R. M. Chrenko, Infrared Absorption from $L \cdot S$ Splittings in Co^{2+} Salts, *Phys. Rev.* **115**, 1147 (1959).
- [104] M. E. Lines, Magnetic properties of CoF_2 , *Phys. Rev.* **137**, A982 (1965).
- [105] K. Häussler, A. Lehmeier, and L. Merten, Far-Infrared Reflectivity of Optical Magnons in FeF_2 and CoF_2 , *Phys. Status Solidi B* **111**, 513 (1982).
- [106] F. M. Johnson and A. H. Nethercot, Antiferromagnetic Resonance in MnF_2 , *Phys. Rev.* **114**, 705 (1959).
- [107] J. L. Duarte, J. A. Sanjurjo, and R. S. Katiyar, Off-normal infrared reflectivity in uniaxial crystals: α - LiIO_3 and α -quartz, *Phys. Rev. B* **36**, 3368 (1987).
- [108] S. J. Allen and H. J. Guggenheim, Spin-Optical-Phonon Interaction in Antiferromagnetic CoF_2 , *Phys. Rev. Lett.* **21**, 1807 (1968).
- [109] S. J. Allen and H. J. Guggenheim, Magnon-Optical Phonon Interaction in Antiferromagnetic CoF_2 , *J. Appl. Phys.* **40**, 999 (1969).
- [110] D. L. Mills and S. Ushioda, Exciton—Optical-Phonon Coupling in CoF_2 , *Phys. Rev. B* **2**, 3805 (1970).
- [111] S. J. Allen Jr and H. J. Guggenheim, Spin waves and excitons in antiferromagnetic CoF_2 , *J. Appl. Phys.* **42**, 1657 (1971).
- [112] F. Gervais and H. Arend, Long-wavelength phonons in the four phases of $\{\text{N}(\text{CH}_3)_4\}_2\text{CuCl}_4$ and effective charges, *Z. Physik B - Condensed Matter* **50**, 17 (1983).
- [113] J. K. Vassiliou, Pressure and temperature dependence of the static dielectric constants and elastic anomalies of ZnF_2 , *J. Appl. Phys.* **59**, 1125 (1986).
- [114] R. Lowndes and D. Martin, Dielectric constants of ionic crystals and their variations with temperature and pressure, Proceedings of the Royal Society of London. A. Mathematical and Physical Sciences **316**, 351 (1970).
- [115] R. A. Bartels and P. A. Smith, Pressure and Temperature Dependence of the Static Dielectric Constants of KCl , NaCl , LiF , and MgO , *Phys. Rev. B* **7**, 3885 (1973).
- [116] M. Wintersgill, J. Fontanella, C. Andeen, and D. Schuele, The temperature variation of the dielectric constant of "pure" CaF_2 , SrF_2 , BaF_2 , and MgO , *J. Appl. Phys.* **50**, 8259 (1979).
- [117] D. L. Fox, D. R. Tilley, J. F. Scott, and H. J. Guggenheim, Magnetoelectric phenomena in BaMnF_4 and $\text{BaMn}_{0.99}\text{Co}_{0.01}\text{F}_4$, *Phys. Rev. B* **21**, 2926 (1980).
- [118] M. S. Seehra and R. E. Helmick, Dielectric anomaly in MnO near the magnetic phase transition, *Phys. Rev. B* **24**, 5098 (1981).
- [119] I. R. Jahn, Linear Magnetic Birefringence in the Antiferromagnetic Iron Group Difluorides, *Phys. Status Solidi B* **57**, 681 (1973).
- [120] P. A. Markovin and R. V. Pisarev, Magnetic, thermal, and elastic refraction of light in the antiferromagnet MnF_2 , *JETP* **50**, 1190 (1979).
- [121] R. M. Dubrovin, A. C. Garcia-Castro, N. V. Siverin, N. N. Novikova, K. N. Boldyrev, A. H. Romero, and R. V. Pisarev, Incipient geometric lattice instability of cubic fluoroperovskites, *Phys. Rev. B* **104**, 144304 (2021).
- [122] A. Kumar, C. J. Fennie, and K. M. Rabe, Spin-lattice coupling and phonon dispersion of CdCr_2O_4 from first principles, *Phys. Rev. B* **86**, 184429 (2012).
- [123] K. Momma and F. Izumi, *VESTA 3* for three-dimensional visualization of crystal, volumetric and morphology data, *J. Appl. Crystallogr.* **44**, 1272 (2011).
- [124] J. A. Barreda-Argüeso, S. López-Moreno, M. N. Sanz-Ortiz, F. Aguado, R. Valiente, J. González, F. Rodríguez, A. H. Romero, A. Muñoz, L. Nataf, and F. Baudelet, Pressure-induced phase-transition sequence in CoF_2 : An experimental and first-principles study on the crystal, vibrational, and electronic properties, *Phys. Rev. B* **88**, 214108 (2013).
- [125] C. Lee, P. Ghosez, and X. Gonze, Lattice dynamics and dielectric properties of incipient ferroelectric TiO_2 rutile, *Phys. Rev. B* **50**, 13379 (1994).
- [126] A. Raeliarijaona and H. Fu, Mode sequence, frequency change of nonsoft phonons, and LO-TO splitting in strained tetragonal BaTiO_3 , *Phys. Rev. B* **92**, 094303 (2015).
- [127] K. D. Fredrickson, C. Lin, S. Zollner, and A. A. Demkov, Theoretical study of negative optical mode splitting in LaAlO_3 , *Phys. Rev. B* **93**, 134301 (2016).
- [128] M. Schubert, A. Mock, R. Korlacki, and V. Darakchieva, Phonon order and reststrahlen bands of polar vibrations in crystals with monoclinic symmetry, *Phys. Rev. B* **99**, 041201 (2019).
- [129] E. Granado, A. García, J. A. Sanjurjo, C. Rettori, I. Torriani, F. Prado, R. D. Sánchez, A. Caneiro, and S. B. Oseroff, Magnetic ordering effects in the raman spectra of $\text{La}_{1-x}\text{Mn}_{1-x}\text{O}_3$, *Phys. Rev. B* **60**, 11879 (1999).
- [130] W. Zhong, R. D. King-Smith, and D. Vanderbilt, Giant LO-TO Splittings in Perovskite Ferroelectrics, *Phys. Rev. Lett.* **72**, 3618 (1994).
- [131] M. Khedidji, D. Amoroso, and H. Djani, Microscopic mechanisms behind hyperferroelectricity, *Phys. Rev. B* **103**, 014116 (2021).
- [132] R. A. Cowley, O. W. Dietrich, and D. A. Jones, Magnetic excitations of mixed $\text{CoF}_2/\text{ZnF}_2$ crystals, *J. Phys. C: Solid State Phys.* **8**, 3023 (1975).
- [133] S. López-Moreno, A. Romero, J. Mejía-López, and A. Muñoz, First-principles study of pressure-induced structural phase transitions in MnF_2 , *Phys. Chem. Chem. Phys.* **18**, 33250 (2016).
- [134] M. Fechner and N. A. Spaldin, Effects of intense optical phonon pumping on the structure and electronic properties of yttrium barium copper oxide, *Phys. Rev. B* **94**, 134307 (2016).

- [135] M. Fechner, A. Sukhov, L. Chotorlishvili, C. Kenel, J. Berakdar, and N. A. Spaldin, Magnetophononics: Ultrafast spin control through the lattice, *Phys. Rev. Mater.* **2**, 064401 (2018).
- [136] A. S. Disa, J. Curtis, M. Fechner, A. Liu, A. von Hoegen, M. Först, T. F. Nova, P. Narang, A. Maljuk, A. V. Boris, B. Keimer, and A. Cavalleri, Photo-induced high-temperature ferromagnetism in YTiO_3 , *Nature* **617**, 73 (2023).
- [137] A. G. Gurevich and G. A. Melkov, *Magnetization oscillations and waves* (CRC, 1996).
- [138] X.-Y. Chen and Y.-P. Wang, One-dimensional model for coupling between magnon and optical phonon, *Phys. Rev. B* **104**, 155132 (2021).
- [139] L.-W. Wang, L.-S. Xie, P.-X. Xu, and K. Xia, First-principles study of magnon-phonon interactions in gadolinium iron garnet, *Phys. Rev. B* **101**, 165137 (2020).
- [140] K. Wang, K. Ren, Y. Hou, Y. Cheng, and G. Zhang, Magnon-phonon coupling: from fundamental physics to applications, *Phys. Chem. Chem. Phys.* **25**, 21802 (2023).
- [141] H. Liu, J. Chaloupka, and G. Khaliullin, Kitaev Spin Liquid in 3d Transition Metal Compounds, *Phys. Rev. Lett.* **125**, 047201 (2020).
- [142] X. Hong, M. Gillig, R. Hentrich, W. Yao, V. Kocsis, A. R. Witte, T. Schreiner, D. Baumann, N. Pérez, A. U. B. Wolter, Y. Li, B. Büchner, and C. Hess, Strongly scattered phonon heat transport of the candidate Kitaev material $\text{Na}_2\text{Co}_2\text{TeO}_6$, *Phys. Rev. B* **104**, 144426 (2021).
- [143] X. Li, Y. Gu, Y. Chen, V. O. Garlea, K. Iida, K. Kamazawa, Y. Li, G. Deng, Q. Xiao, X. Zheng, Z. Ye, Y. Peng, I. A. Zaliznyak, J. M. Tranquada, and Y. Li, Giant Magnetic In-Plane Anisotropy and Competing Instabilities in $\text{Na}_3\text{Co}_2\text{SbO}_6$, *Phys. Rev. X* **12**, 041024 (2022).
- [144] K. Feng, S. Swarup, and N. B. Perkins, Footprints of Kitaev spin liquid in the Fano lineshape of Raman-active optical phonons, *Phys. Rev. B* **105**, L121108 (2022).
- [145] N. Li, R. R. Neumann, S. K. Guang, Q. Huang, J. Liu, K. Xia, X. Y. Yue, Y. Sun, Y. Y. Wang, Q. J. Li, Y. Jiang, J. Fang, Z. Jiang, X. Zhao, A. Mook, J. Henk, I. Mertig, H. D. Zhou, and X. F. Sun, Magnon-polaron driven thermal Hall effect in a Heisenberg-Kitaev antiferromagnet, *Phys. Rev. B* **108**, L140402 (2023).
- [146] S. Zhang, S. Lee, A. J. Woods, W. K. Peria, S. M. Thomas, R. Movshovich, E. Brosha, Q. Huang, H. Zhou, V. S. Zapf, and M. Lee, Electronic and magnetic phase diagrams of the Kitaev quantum spin liquid candidate $\text{Na}_2\text{Co}_2\text{TeO}_6$, *Phys. Rev. B* **108**, 064421 (2023).